

3D Printing of $\text{Li}_{6.4}\text{La}_3\text{Zr}_{1.4}\text{Ta}_{0.6}\text{O}_{12}$

**Zur Erlangung des akademischen Grades eines
DOKTORS DER INGENIEURWISSENSCHAFTEN (DR.-ING.)**

**von der KIT-Fakultät für Chemieingenieurwesen und Verfahrenstechnik des
Karlsruher Instituts für Technologie (KIT)
genehmigte**

DISSERTATION

von

M. Sc. Bo Chen

aus Jilin, China

Tag der mündlichen Prüfung: 24.04.2023

Erstgutachter: Prof. Dr. Norbert Willenbacher

Zweitgutachter: Prof. Dr.-Ing. Christoph Klahn

Acknowledgements

This thesis was done at the Institute of Mechanical Process Engineering and Mechanics at the Karlsruhe Institute of Technology (KIT). The completion of this thesis is inseparable from the support of many people. In particular, I would like to thank the China Scholarship Council (CSC) for financially supporting me during my stay in Germany.

First of all, I would like to express my sincere thanks and appreciation to my supervisor, Prof. Dr. Norbert Willenbacher, for his constant support, guidance, motivation and profound knowledge. I appreciate the opportunity to work in his interdisciplinary group providing a creative working atmosphere. I am further grateful for the opportunity to participate in scientific conferences, seminars and discussions.

My sincere thanks go to my second supervisor, Prof. Dr.-Ing. Christoph Klahn of Karlsruhe Institute of Technology, for his advice and support. In addition, I would like to thank Dr.-Ing. Claude Oelschlaeger and Dr. Bernhard Hochstein and Dr. Wang Yiliang taught me knowledge and guided my research in rheology, 3D printing and other related fields.

I would also like to thank Dr. Moritz Weiß and David Menne, for all their discussions and advice on experiments in the field of ceramics.

Special thanks go to my colleagues and friends Dr. Xu Chenhui, Dr. Nie Shouliang, Bruna Regina Maciel and Han Zongyou for their invaluable support, scientific and non-scientific discussions, and constant encouragement.

I am also very grateful to Dr. Yunlong Zhang and Dr. Qiang Fu for their sincere friendship and cheering me up to share incredible moments together. We would also like to thank Dr. Yong Hu for his help and support.

I am very grateful to Kevin Tedjokusuma for his discussion and communication in the field of sintering, to Ophélie Ranquet for her support on compressive strength measurements, to Karim Abdel Aal for his guidance on capillary rheometry, to Max Ailinger for his guidance on contact angle measurement experiments, and to Katrin Dyhr's support in the IT field, thanks to Katarzyna Pesta for the communication in the battery field. Thanks are given to Thomas Lebe for the support at the SEM microscope

Many thanks to Felipe Mello Rigon, Dr. Johanna Roether, Dr. Hongye Sun, Dr. Frank Bossler, Dr. Ronald Gordon, Dr. Walter Oswald, Dr. Ceren Yüce, Annika Hodapp, Jonas Marten, Wolf Gereon Wedel and other colleagues for their support while working and living in Germany.

Last but not least, I would like to thank my wife Dr. Qiyang Jiang and my family for their support and encouragement in completing my Ph.D. work.

Abstract

$\text{Li}_{6.4}\text{La}_3\text{Zr}_{1.4}\text{Ta}_{0.6}\text{O}_{12}$ (LLZTO), as an element-doped garnet-type solid electrolyte material, has become one of the most promising ceramic solid electrolyte materials with its high ionic conductivity and high stability to lithium metal. However, in terms of processing LLZTO materials, the traditional casting method is still the mainstream processing technology. The lack of shape diversity and structural complexity when manufacturing LLZTO materials by this traditional methods greatly limits the development and progress of solid electrolytes. Here, three LLZTO ink formulations are presented to successfully print complex high-precision ($150\ \mu\text{m}$) 3D structures by direct ink writing, where the structures include hexagonal honeycomb, triangular, and square log-pile structures. Based on the ink's specially tailored rheological properties, such as pronounced shear-thinning behavior, high modulus $G' > 10^5\ \text{Pa}$, and high yield stress $\sigma_y \approx 1000\ \text{Pa}$, these rheological properties contribute to the excellent printing performance of the ink. Based on these inks, LLZTO materials can be 3D printed into three-dimensional complex solid electrolytes with controllable precision and free design.

Zusammenfassung

$\text{Li}_{6.4}\text{La}_3\text{Zr}_{1.4}\text{Ta}_{0.6}\text{O}_{12}$ (LLZTO) ist als elementdotiertes granatartiges Festelektrolytmaterial mit seiner hohen Ionenleitfähigkeit und hohen Stabilität gegenüber Lithiummetall ein vielversprechender keramischer Werkstoff für Li-Ionen Batterien. Allerdings dominieren bei der Verarbeitung von LLZTO nach wie vor herkömmliche Verarbeitungsmethoden wie das Fließpressverfahren. In Bezug auf die Verarbeitung von LLZTO-Materialien ist dieses traditionelle Gießverfahren immer noch die Hauptverarbeitungstechnologie. Der Mangel an Formenvielfalt und struktureller Komplexität bei der Herstellung von LLZTO-Materialien durch diese herkömmlichen Verfahren schränkt die Entwicklung und den Fortschritt von Festelektrolyten stark ein. Hier werden drei LLZTO-Tintenformulierungen vorgestellt, mit denen es erfolgreich möglich war komplexe hochpräzise ($150\ \mu\text{m}$) 3D-Strukturen durch direktes Tintenschreiben zu drucken, wobei die Strukturen sechseckige Waben-, dreieckige und runde Pfahlquadratstrukturen umfassen. Basierend auf den speziell abgestimmten rheologischen Eigenschaften der Tinte, wie ausgeprägte Strukturviskosität, hoher Modul $G' > 10^5\ \text{Pa}$ und hohe Fließgrenze $\sigma_y \approx 1000\ \text{Pa}$, tragen diese rheologischen Eigenschaften zur hervorragenden Druckbarkeit der Tinte bei. Basierend auf diesen Tinten können LLZTO-Materialien mit kontrollierbarer Präzision und freiem Design zu dreidimensionalen komplexen Festelektrolyten 3D-gedruckt werden.

List of symbols

ρ	Density	g cm^{-3}
t	Time	s
θ	Contact angle	$^{\circ}$
d	Diameter	mm
G	Modulus	Pa
h	Height	mm
v	Velocity	mm s^{-1}
$\dot{\gamma}$	Shear rate	s^{-1}
γ	Strain	-
φ	Volume fraction	%
ε	Porosity	%
ε^*	True porosity	%
ω	Angular frequency	rad s^{-1}
σ_y	Yield stress	Pa
g	Gravity	g cm^{-3}
X_{50}	Pore size	μm
T	Temperature	$^{\circ}\text{C}$
η	Viscosity	Pa s
L	Length	Mm
K	Flow consistency index	
τ	Shear stress	N m^{-2}
m	Dimensionless thixotropic exponent	
n	Flow index	
rpm	Rounds per minute	min^{-1}
DIW	Direct Ink Writing	
FDM	Fused Deposition Modeling	
SLA	Stereolithography apparatus	
XRD	X-ray diffraction	
EDS	X-ray spectroscopy	
SEM	Scanning electron microscopy	
LSM	Laser scanning microscope	
PDMS	Polydimethylsiloxane	
DMF	N,N-dimethylformamide	

Index

Acknowledgements	II
Abstract	IV
Zusammenfassung	V
List of symbols	VI
Introduction	1
1.1 Background and motivation	1
1.2 Outline of this work.....	3
State of the art and literature review	4
2.1 Lithium-ion battery	4
2.1.1 Lithium-ion battery overview	4
2.1.2 Li-ion battery electrolyte.....	6
2.1.3 Solid-state electrolytes.....	9
2.2 Additive Manufacturing	16
2.3 Additive manufacturing solid-state electrolytes.....	18
2.3.1 Direct Ink Writing.....	19
2.3.2 Stereolithography.....	20
2.3.3 Fused Deposition Modeling	22
Materials and sample preparation	24
3.1 Materials.....	24
3.1.1 Particles	24
3.1.2 Additives	26
3.1.3 Solvents.....	27
3.2 Ink preparation	29
3.2.1 Speed mixer.....	29
3.2.2 Three roll mill	30
3.3 Formulations.....	32
Methodology	34
4.1 Contact angle	34
4.2 Rheological measurements	35
4.2.1 Yield stress measurement.....	35
4.2.2 Viscosity.....	37
4.2.3 Modulus	39
4.2.4 Slip velocity.....	40
4.3 3D printing	40

4.3.1 Direct Ink Writing (DIW)	40
4.3.2 Stereo lithography apparatus (SLA).....	41
4.3.3 Fused deposition modeling (FDM).....	42
4.4 Sintering	43
4.5 Structural Characterization	44
4.6 Mechanical Measurements.....	45
Results and discussion	46
5.1 DIW 3D printing LLZTO	46
5.1.1 Capillary suspension.....	46
5.1.2 Rheological properties of DIW inks.....	47
5.1.3 Structural features of DIW 3D printed samples	57
5.1.4 Sintering and characterization of samples	59
5.1.5 Mechanical properties of DIW 3D printed samples	66
5.2 SLA 3D printing LLZTO	70
5.3 FDM 3D printing LLZTO	71
Conclusions	78
Outlook	80
References	82

Chapter 1:

Introduction

1.1 Background and motivation

Lithium batteries play an important role as a major alternative to non-renewable resources such as fossil fuels. Since their commercialization in the early 1990s, lithium batteries have grown rapidly due to their long cycle life and high energy density. In just a few years, they have been used in every aspect of everyone's life, such as cell phones, laptops, etc. Today, they are used as green energy storage devices, making a prominent contribution to the reduction of CO₂ emissions.[1-3]

However, with the rapid expansion of traditional Li-ion batteries, flammable organic liquid electrolytes or polymer electrolytes are likely to cause safety problems such as explosions due to poor thermal stability and low ignition point. Solid-state lithium-ion batteries provide a possible way to solve safety problems by using solid-state electrolytes with high thermal stability instead of flammable organic liquid electrolytes.[4-7] There are many inorganic materials suitable for solid electrolytes, including sulfide-type, NASICON-type, perovskite-type, and garnet-type materials.[8] Garnet-type electrolyte material has attracted extensive attention since the first discovery in 1969 because of their high electrochemical oxidation voltage, high mechanical strength, high chemical and electrochemical stability.[9] The high ion conductivity of $1.02 \times 10^{-3} \text{ S cm}^{-1}$ was achieved using LLZTO material as SSE at room temperature, which provides the possibility for further breakthroughs in lithium battery materials. This work was reported by Murugan et al.[10]

In the industry, large-scale production of inorganic solid electrolytes has been

achieved through traditional processing techniques such as tape casting.[11, 12] However, although these methods reduce costs, they can only produce solid electrolytes with a given thickness of lamellar structures, which greatly limits the application and development of solid-state electrolytes. Realizing the flexibility of size and the complexity of the electrolyte structure has become a updated challenge for the development of solid-state electrolyte.

As an additive manufacturing method, 3D printing has the characteristics of precise and diverse configurations, fast finished products. This provides more possibilities for flexibly controlling the size of the structure and manufacturing three-dimensional and complex spatial structures.[13] Successful 3D printing of inorganic solid electrolyte materials requires tailor-made inks that are compliant, and Smay et al. [14, 15] demonstrated that printable inks should exhibit appropriate rheological properties.

In this context, this thesis aims to develop well-printable inks for inorganic solid electrolyte materials and demonstrate the structural diversity and size flexibility of solid electrolytes that can be achieved using these inks.

1.2 Outline of this work

After the brief introduction to this thesis in section 1.1, based on the corresponding objectives, the thesis is organized as follows:

In chapter 2, background of solid-state Li-ion batteries is introduced, including the development and challenges of solid-state lithium-ion batteries, the advantages and limitations of solid-state electrolyte materials, and the processing characteristics of different types of materials. It briefly describes the 3D printing process, including the types and process characteristics of 3D printing. Finally, in this chapter, the composition of the ink which affects the flow and hence printing properties is outlined.

In chapter 3, the materials used in the paper are introduced in detail, and two different types of inks are designed for DIW 3D printing, one is a capillary suspension ink and the other is a dispersant ink. The ink manufacturing process and manufacturing methods are introduced in detail.

In chapter 4, the rheological methods used to characterize the inks are presented, together with the structural characterization of the printed objects, and finally the mechanical properties of the sintered objects are described.

In chapter 5, the printability of 3D printing solid electrolyte ink is summarized and discussed, and the most suitable printing ink is obtained through the analysis of rheological properties of the different inks. After 3D printing, the structural characterizations of the samples were carried out, and finally the mechanical properties of the sintered objects were tested to complete the set goal and realize the 3D printing of solid electrolyte materials.

In chapter 6 and **chapter 7**, the final discussion of the thesis is summarized and the outlook of 3D printing solid electrolytes is prospected.

Chapter 2:

State of the art and literature review

2.1 Lithium-ion battery

2.1.1 Lithium-ion battery overview

Lithium-ion batteries are commonly used in all aspects of life today as rechargeable energy storage devices.[3] Lithium ions and electrons are ionized from the lithium atoms in the cathode, and the lithium ions eventually move to the anode to synthesize lithium atoms with electrons. This phenomenon is known as the charging process of Li-ion batteries.[16] Lithium atoms are ionized into Li-ions and electrons in the anode. Lithium ions pass through the electrolyte from the anode, and finally transfer to the cathode, where the electrons recombine with the Li-ions and complete electrical neutralization at the cathode of the Li-ion battery. This process is the Li-ion battery discharge process. (see Fig. 2.1) [17] The main components of the Li-ion batteries are negative electrode, electrolyte, anode and separator. They are also known as the four main materials of lithium batteries.

Cathode (negative electrode): Lithium-containing transition metal oxides are generally used.[18]

Anode (positive electrode): It is usually formed by mixing carbon materials or non-carbon materials, binders and additives as the active materials, and on both sides of the copper foil are evenly spread the paste, finally dry and roll the paste. The main body of lithium-ion batteries storing lithium are the negative electrode materials, and the process of extracting and intercalated lithium ions is the discharging and charging process of the negative electrode materials. [19]

Electrolyte: a medium substance that helps lithium ions transfer smoothly.[20]

Separator: separate the negative electrodes and the positive electrodes of the batteries through the closed cell function to prevent direct contact and short circuit, which can block the conduction of current and prevent the battery from overheating or even exploding.[21]

The working principle of the Li-ion batteries are based on their charging and discharging process. The process of lithium ions (Li^+) released from the cathodes being transferred to the positive electrode through the electrolyte is the charging process of the lithium-ion battery. Usually the anodes are layered and have many micropores. When the anodes get lithium ions, these micropores intercalate lithium ions into them. The charging capacity of the Li-ion batteries is determined by the number of lithium ions intercalated. The chargeability of the battery increases with the number of intercalated ions. [22]

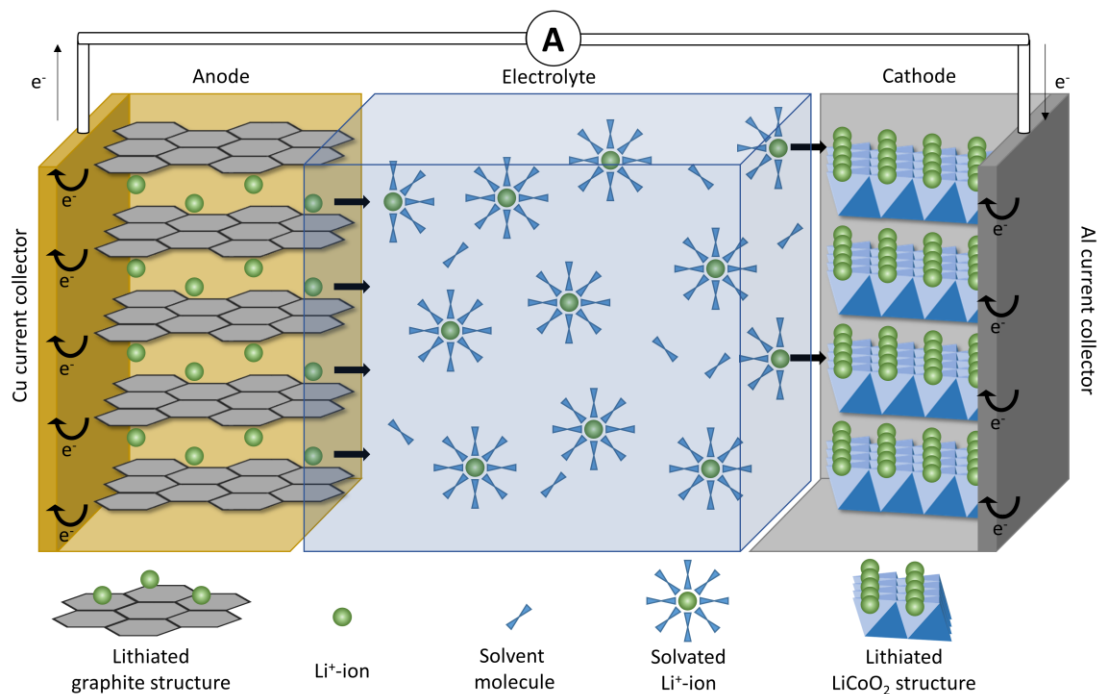


Fig. 2.1 Schematic diagram of a lithium-ion battery.[23]

Reversing charging processes are the discharging processes of Li-ion batteries.

The electrolyte dissociates Li-ions from the anode to the cathode, and the discharge capacity increases with the increase of Li-ions reaching the cathode. Discharge capacity is also known as batteries capacity.[24]

M. Stanley Whittingham prepared the first lithium-ion battery in the 1970s by using metallic lithium as the negative electrodes, TiS_2 as the positive electrodes.[25] However, this lithium-ion battery is extremely flammable and has great safety hazards. In the 1980s, J.B. Goodenough and others successively discovered negative electrode materials such as LiCoO_2 and manganese spines, which can improve the safety of Li-ion battery, thus, made great contributions to the commercialization of the Li-ion battery.[26] In another work, the complete elimination of metallic lithium was achieved by Akira Yoshino's in 1985. More importantly, they established the basic concept of a rechargeable lithium-containing alkaline lithium-ion battery (LIB).[27] In order to reward them for their outstanding contributions to the Li-ion battery, they were awarded the Chemistry of Nobel Prize in 2019.

Excellent cathode and anode materials have been discovered by more and more people, so this thesis will not go into details. Based on the goal of this thesis, the discussion will focus on lithium-ion battery electrolytes, because the research of lithium-ion electrolytes still has great prospects, such as the innovation of solid-state electrolyte processing technology, or the development of structural design.

2.1.2 Li-ion battery electrolyte

Wide electrochemical windows, good thermal stability and high ion conductivity in a wide temperature range are the characteristics that lithium-ion battery electrolytes should possess.[28]

According to the state of the Li-ion batteries electrolytes, they can generally be

divided into solid-liquid-state mixed electrolytes, solid-state electrolytes (SSE) and liquid electrolytes.[29] Generally, gel-state electrolytes composed of liquid electrolytes and solid polymers are composite solid-liquid-state electrolytes. Both inorganic SSE and polymer SSE are solid electrolytes. Room temperature ionic liquid electrolytes and organic liquid electrolytes are liquid electrolytes. Fig. 2.2 shows the relationship between the ion conductivity of different SSE and the suitable voltage window at room temperature.

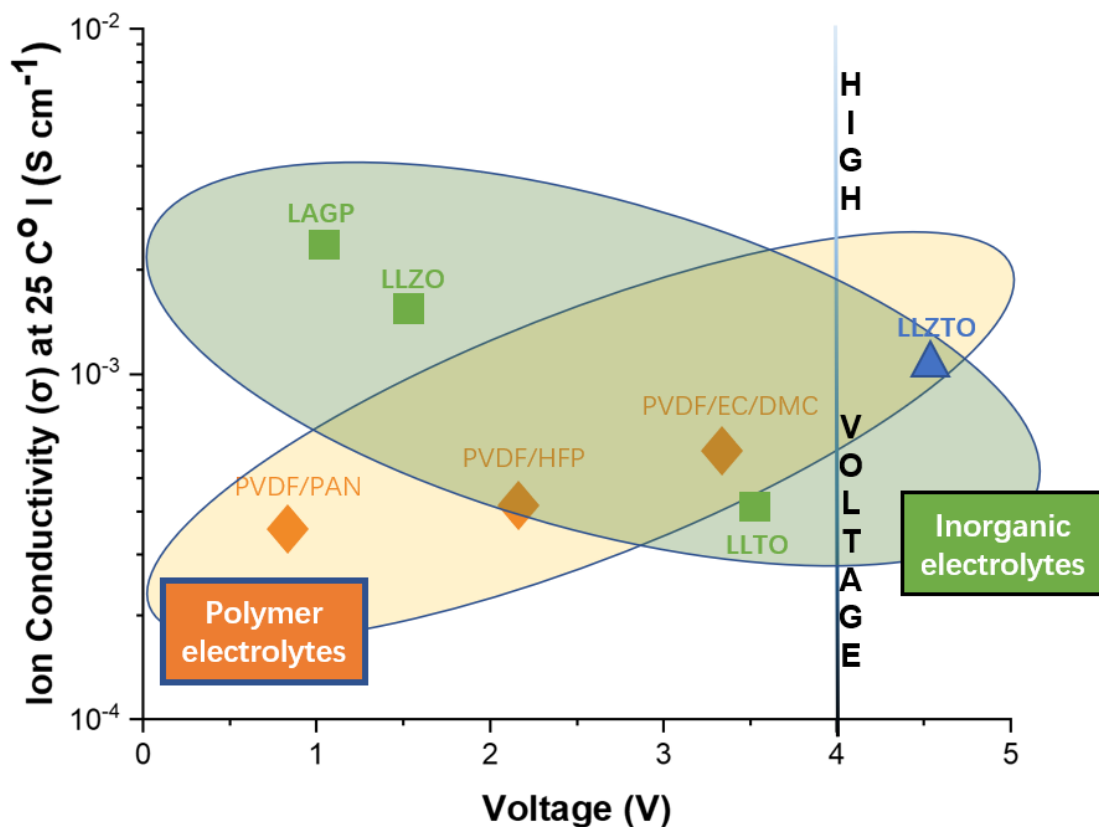


Fig. 2.2 The relationship between the ion conductivity of different SSEs and the suitable voltage window at room temperature.[29]

Organic liquid electrolyte

Organic liquid electrolytes are obtained by dissolving different lithium salts in polar aprotic organic solvents.[30] This type of electrolytes have high boiling point, low freezing point and good electrochemical stability. But the organic

liquid electrolytes have high viscosity, low conductivity, small dielectric constants, poor ability to dissolve inorganic salts, and are particularly sensitive to trace amounts of water. Organic liquid-state Li-ion battery is prone to leakage. The flammability of organic solvent can make Li-ion battery less safe. Therefore, perfect protection measures are necessary for liquid lithium-ion batteries. Typically, the liquid electrolyte is encased in a metal casing of fixed dimensions.[31]

Room temperature ionic liquid (RTILs)-based electrolyte

Nowadays, RTILs are the most common electrolyte. RTILs-based electrolyte is a functional material or medium that is liquid at room temperature and is composed of specific cations and anions. RTILs-based electrolytes have newly received much more attention due to the significant advantages of low vapor pressure, high conductivity, wide liquid range, good electrochemical stability, easy recycling, and without pollution.[32] At high power densities and completely eliminate potential safety hazards of Li-ion battery, the room temperature molten salts are used as the electrolyte of Li-ion battery to improve their safety, thus making it possible for lithium-ion batteries to be used in large power systems such as electric vehicles or under other special conditions.

Solid polymer electrolyte (SPEs)

Solid polymer electrolytes have the advantages of nonflammability, low reactivity with electrode materials, and good flexibility. [33] These advantages can surmount the hereinabove-mentioned disadvantages of liquid-state Li-ion batteries. Solid electrolytes allow the volume changes during discharge of electrode materials and are resistant to shock, deformation than liquid-state electrolytes, and vibration. The solid electrolytes are convenience to process and shape, and the different shapes of Li-ion batteries according to different needs can be made.

Gel polymer electrolyte

Introduce liquid plasticizers such as Polycarbonate, Ethylene carbonate, etc. into the polymer to obtain a solid-liquid-state composite gel-like electrolytes. This hybrid electrolytes composed of lithium salts, polymer compounds and polar organic solvents have both properties of solid electrolytes and liquid electrolytes.[34]

Inorganic solid-state electrolyte

Inorganic solid-state electrolytes for solid Li-ion batteries are mainly divided into ceramic electrolytes and glass electrolytes. Solid-state electrolytes function as electrolytes and can replace diaphragms in batteries. Therefore, inorganic solid electrolytes are used to prepare SSE Li-ion batteries without liquid leakage, and the Li-ion batteries can be miniaturized. Although the lithium ions migration number are larger in this kind of material, the ion conductivity of the electrolytes themselves are much smaller than that of the liquid electrolytes. When the materials are used in the Li-ion battery, the interface resistance between the electrode materials and the electrolyte materials is high. In addition, the brittleness of the inorganic SSE is high, and the shock resistance of the Li-ion battery as the electrolyte is poor. [8]

In the past several years, most researches on Li-ion batteries have focused on liquid electrolyte systems.[35]

The aim of this thesis is on solid-state electrolytes and how they can be processed to obtain complex solid structures.

2.1.3 Solid-state electrolytes

Solid-state electrolyte is used to cope with the challenges of dendrite growth in

metal anodes of liquid electrolyte lithium-ion batteries that may lead to thermal runaway as well as poor cycle life and low coulombic efficiency.[36]

Mechanism of ionic transport in solids

According to the different Li-ion transport modes in SSE, solid electrolytes have two categories: inorganic materials and polymers. In crystalline materials, the temperature dependence of ion conductivity is generally modeled by Arrhenius, and in amorphous materials by the Vogel Tamman Fulcher (VTF) equation.[37] In polymer solid electrolytes, ions jump from one coordination site to another under the action of an electric field to realize ion conduction. Segmental motion is possible with the help of amorphous polymer chains above the glass transition temperature (T_g). Therefore, the ionic conductivity of polymers in solid electrolytes depends largely on their crystallinity.[38, 39] For crystalline inorganic material-based electrolytes, ions transport are achieved through their defect sites, and the distribution and concentration of defect sites will affect ion diffusion. The ions diffusion mechanisms ground on Frenkel point defects and Schottky have two categories: one is vacancy mediated and includes vacancy and divacancy mechanisms. The other one is a gap mediated process and includes gap mechanisms, gap displacement exchange mechanisms and collective mechanisms.[40-42] For ion transport in glassy inorganic materials, it works similarly to crystalline materials.[43]

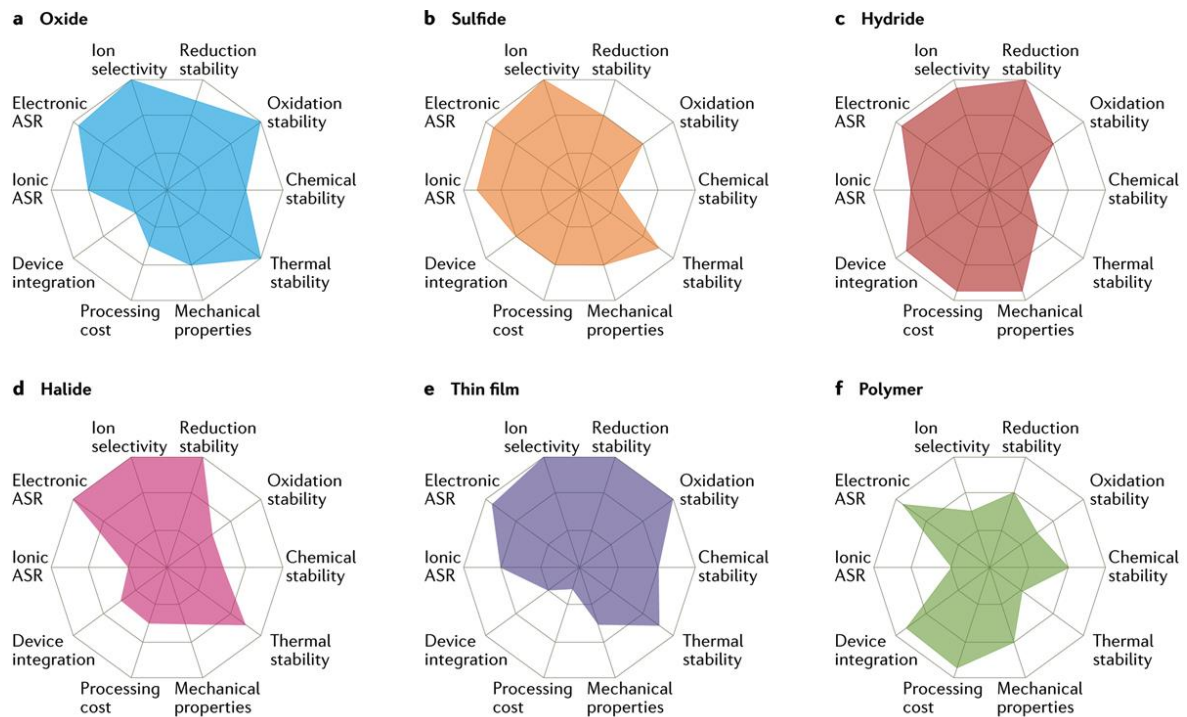
Solid electrolyte materials

Materials used as solid-state electrolytes mainly need to meet the following properties: low ionic area specific resistance (ASR), high electronic ASR, excellent mechanical properties, high ion conductivity, high ion selectivity, wide electrochemical stability window, excellent thermal stability, low cost, simple manufacturing process and environmental friendliness.[44-48] Polymer and

inorganic solid electrolyte materials have made great progress in improving the above properties. Table 2.1 summarizes the available solid electrolyte materials, and Fig. 2.3 visualizes the above-mentioned material properties in a radar diagram.

Table 2.1 Summary of lithium-ion solid electrolyte materials.[8]

Type	Materials	Conductivity (S cm ⁻¹)	Advantages	Disadvantages
Oxide	Perovskite Li ₃₃ La _{0.56} TiO ₃ NASICON LiTi ₂ (PO ₄) ₃ LISICON Li ₁₄ Zn(GeO ₄) ₄ Garnet Li ₇ La ₃ Zr ₂ O ₁₂	10 ⁻⁵ -10 ⁻³	<ul style="list-style-type: none"> High chemical and electrochemical stability High mechanical strength High electrochemical oxidation voltage 	<ul style="list-style-type: none"> Non-flexible Expensive large-scale production
Sulfide	Li ₂ S-P ₂ S ₅ Li ₂ S-P ₂ S ₅ -MS _x	10 ⁻⁷ -10 ⁻³	<ul style="list-style-type: none"> High conductivity Good mechanical strength and mechanical flexibility 	<ul style="list-style-type: none"> Low oxidation stability Sensitive to moisture
Hydride	LiBH ₄ , LiBH ₄ -LiX LiNH ₂ , Li ₃ AlH ₆	10 ⁻⁷ -10 ⁻⁴	<ul style="list-style-type: none"> Low grain-boundary resistance Stable with lithium metal 	<ul style="list-style-type: none"> Sensitive to moisture
Halide	LiI, spinel LiZnI ₄ Anti-perovskite Li ₃ OCl	10 ⁻⁸ -10 ⁻⁵	<ul style="list-style-type: none"> Stable with lithium metal Good mechanical strength 	<ul style="list-style-type: none"> Sensitive to moisture
Borate or phosphate	Li ₂ B ₄ O ₇ , LiPO ₄ and Li ₂ O-B ₂ O ₃ -P ₂ O ₅	10 ⁻⁷ -10 ⁻⁶	<ul style="list-style-type: none"> Facile manufacturing process Good durability 	<ul style="list-style-type: none"> Relatively low conductivity
Thin film	LiPON	10 ⁻⁶	<ul style="list-style-type: none"> Stable with lithium metal Stable with cathode materials 	<ul style="list-style-type: none"> Expensive large-scale production
Polymer	PEO	10 ⁻⁴ (65-78°C)	<ul style="list-style-type: none"> Flexible Stable with lithium metal 	<ul style="list-style-type: none"> Limited thermal stability



Nature Reviews | Materials

Fig. 2.3 Performance of different solid electrolyte materials. (a) oxide solid electrolytes; (b) sulfide solid electrolytes; (c) hydride solid electrolytes; (d) halide solid electrolytes; (e) thin-film electrolytes; (f) and polymer solid electrolytes. ASR, area-specific resistance.[8]

Thin-film solid electrolytes

The material is fabricated into an ultra-thin film as a thin-film SSE by methods such as chemical vapor deposition, radio frequency sputtering and pulsed laser deposition. In 1980s, using $\text{Li}_{12}\text{Si}_3\text{P}_2\text{O}_{20}$, $\text{Li}_4\text{P}_2\text{S}_7$ and $\text{Li}_3\text{PO}_4 - \text{P}_2\text{S}_5$ as starting materials, thin-film solid-state electrolytes were first made.[49-51] Subsequently, thin-film SSE ground on lithium phosphate, glassy lithium phosphorus oxynitride, lithium borate and lithium borophosphate glass have been successfully developed.[52-58] Each of these new electrolytes has its own unique advantages.

Polymer solid electrolytes

Polymer solid-state electrolytes have two categories: dry polymer SSEs and composite polymer-state electrolytes. A polymer host is generally used be combined with lithium salts as the dry polymer SSEs.[59-62] The problem of low ionic conductivity at ambient temperature is solved by adding ceramic fillers to dry polymer systems to form composite polymer electrolytes. The polymer host of composite polymer solid-state electrolyte is typically polymethyl methacrylate, polyvinyl chloride an polyvinylidene difluoride, polyacrylonitrile and polyethylene oxide.[63-67] Ceramic fillers contribute to the , ion conductivity, mechanical strength and stability of the interface surface, they are mainly divided into two categories: active and passive.[68-70] The first type of active fillers (Li_2N and LiAlO_2) partially participate in ion conduction,[71-73] and the second type of inactive fillers (Al_2O_3 , SiO_2 and MgO) don't participate in ions transport.[74-76]

Inorganic solid electrolytes

Inorganic SSEs are mainly divided into two categories: sulfides and oxides. Oxide-type materials mainly include NASICON, perovskite and garnet.

Sulfide electrolytes

The $\text{Li}_2\text{S}-\text{SiS}_2$ system is the earliest discovered sulfide-type solid electrolyte.[77, 78] Sulfide-type SSE have high ion conductivity since the high polarizability of sulfide ions weakens the interaction between Li ions and anions. While the chemical stability of the $\text{Li}_2\text{S}-\text{SiS}_2$ system is not good enough. $\text{Li}_2\text{S}-\text{SiS}_2$ and $\text{Li}_2\text{SP}_2\text{S}_5$ based electrolytes, $\text{Li}_{4-x}\text{M}_{1-y}\text{M}'_y\text{S}_4$ ($\text{M}' = \text{Zn}, \text{P}, \text{Al}, \text{Ga}, \text{M} = \text{Ge}, \text{Si}$), thio-LISICON family and other new generation sulfide-type electrolytes have been intensively studied.[79-85]

Oxide electrolytes

NASICON-type

The NASICON-type materials compound was named "NASICON" after $\text{Na}_{1+x}\text{Zr}_2\text{Si}_x\text{P}_{3-x}\text{O}_{12}$ was developed in 1976.[86] High voltage SSE batteries use NASICON materials as the solid electrolyte. These materials typically have molecular formula $\text{AM}_2(\text{PO}_4)_3$, where the A sites are occupied by Na, Li, or K. M sites are usually occupied by Ti, Ge or Zr.[87] Fig. 2.4 shows the NASICON materials structure, which is the framework of $\text{Li}_{1+y}\text{Al}_y\text{Ti}_{2-y}(\text{PO}_4)_3$ (LATP), $\text{LiM}_2(\text{PO}_4)_3$ and $\text{Li}_{1+a}\text{Al}_z\text{Ge}_{2-a}(\text{PO}_4)_3$ (LAGP) with the framework materials are considered to be excellent lithium ion conductors, but they have the problem of instability to the lithium metal anode.[88-92]

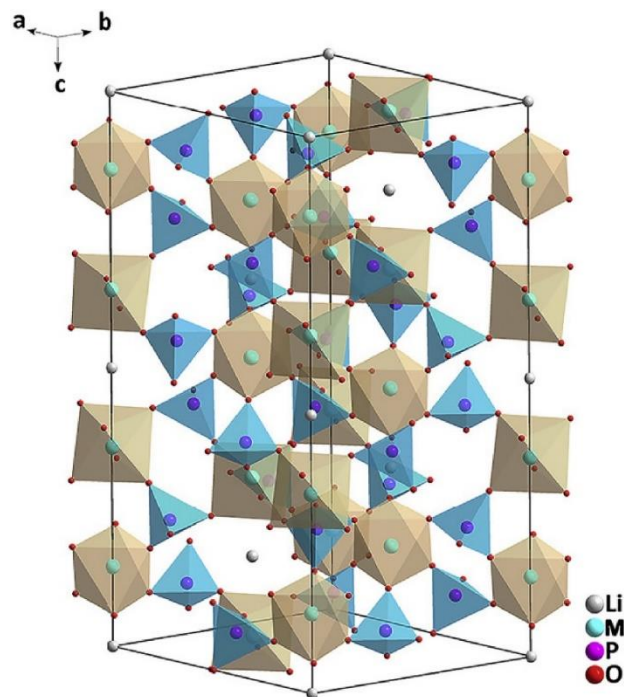


Fig. 2.4 3D NASICON-type structure of $\text{LiM}_2(\text{PO}_4)_3$ [93]

Perovskite-type

The perovskite solid electrolyte refers to a material with a general structural formula of ABO_3 (A = Li, La; B = Ti). It was first reported by Latie et al.[94] Li^+ are transported through defects between A sites in ABO_3 . Fig. 2.5 is a schematic

diagram of ABO_3 . $Li_{3x}La_{2/3-x}TiO_3$ is its representative material.[95] Due to the presence of Ti^{4+} , $Li_{3x}La_{2/3-x}TiO_3$ is readily reduced by metallic lithium anodes and thus considered unsuitable for Li-ion batteries.

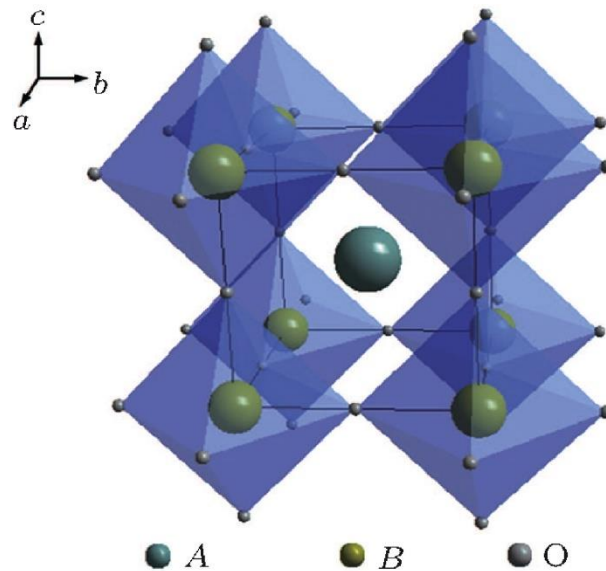


Fig. 2.5 Structure schematic of perovskite-type electrolytes (ABO_3) [96]

Garnet-type

$A_3B_2(XO_4)_3$ is the general formula of garnet-type solid electrolyte materials, where $A = Mg, Ca, Y, La$ or rare earth elements, and which is an 8-coordinated cation. $B = Al, Ge, Mn, Fe, Ga, Ni$, which is a 6-coordinated cation. $X = Si, Ge, Al$, 4 coordination cations. (Fig. 2.6) Since the first discovery of $Li_3M_2Ln_3O_{12}$ ($M = W$ or Te) garnet-type solid electrolyte materials,[9] more and more new materials have been developed. The most representative ones are $Li_5La_3Nb_2O_{12}$, $Li_6BaLa_2Ta_2O_{12}$ and $Li_7La_3Zr_2O_{12}$ (LLZO).[97-100] Among them, LLZO has two different crystal phases, one is cubic phase and the other one is tetragonal phase. Cubic LLZO has higher ionic conductivity than tetragonal LLZO.[101] However, the preparation of cubic LLZO SSE requires high calcination temperature, and the doping of Al, Nb, Te, Ta and other substances in the Li sublattice can help reduce the interfacial resistance problem of SSE

Li-ion batteries.[10, 102-108] Recently, Li et al.[109] discovered $\text{Li}_{6.4}\text{La}_3\text{Zr}_{1.4}\text{Ta}_{0.6}\text{O}_{12}$ (LLZTO) garnet-type SSE materials with an ionic conductivity just like $1.02 \times 10^{-3} \text{ S cm}^{-1}$ at 25°C .

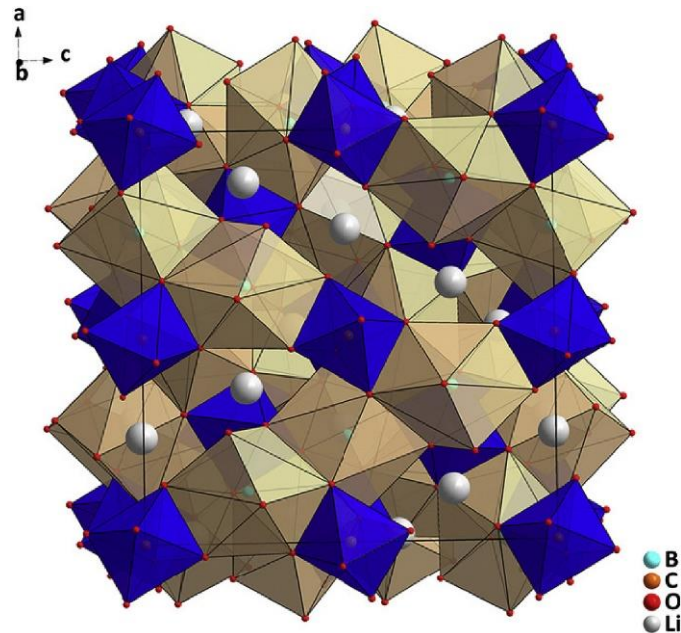


Fig. 2.6 The crystal structure of 3D garnet-type $\text{Li}_3\text{B}_3\text{C}_2\text{O}_{12}$ [93]

Therefore, LLZTO was also chosen as the main solid material in this thesis. Because of the high ion conductivity and wide electrochemical window, the LLZTO material can help to improve the electrolyte properties.

2.2 Additive Manufacturing

Additive manufacturing (AM) is a manufacturing process that builds samples layer-by-layer by digitally controlling the deposition of successive material layers, and finally realizes the manufacture of three-dimensional (3D) structural objects. It is therefore also referred to as 3D printing.[110] Subtractive manufacturing differs from additive manufacturing in that all unnecessary material is removed from the monolithic object in the process of obtaining the final prototype. Objects are usually processed by milling, drilling, sawing and

other processes. Both additive manufacturing and subtractive manufacturing techniques are effective methods for rapid manufacturing prototyping. Simplified schematics of these two fabrication methods are shown in Figure 2.7. According to the complexity of the final sample structure, the characteristics of the selected materials, and the required structural accuracy and cost, etc., the selected manufacturing method is finally determined after comparative analysis. In general, additive manufacturing is suitable for complex designs with multiple hollow parts, because it is simpler and more straightforward to manufacture porous structures by printing solid parts layer by layer. Subtractive manufacturing is more suitable for mass production.

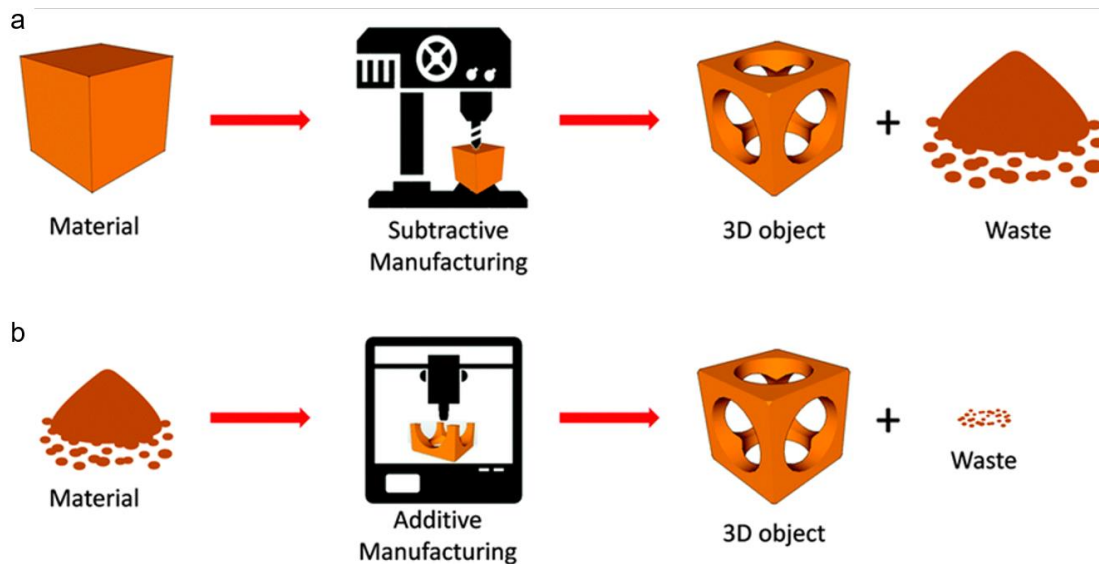


Fig. 2.7 Additive and subtractive manufacturing. (a) In subtractive manufacturing, bulk material is processed through a material removal machine according to a digital design, and a final 3D sample is obtained with a large amount of residual material. (b) In additive manufacturing, starting materials (powders, liquids, filaments, etc.) are processed by a 3D printer, which deposits the material layer by layer, resulting in a 3D sample. The amount of residual material left after this process is significantly lower than that produced by subtractive manufacturing.[111]

In addition, additive manufacturing is widely used in all aspects of life. However,

due to its high production cost, low-cost manufacturing has become the most important challenge at present.

2.3 Additive manufacturing solid-state electrolytes

As an additive manufacturing technology, 3D printing has the ability to manufacture the required complex structures; precisely control the shape and thickness of electrodes; print solid electrolytes with high structural stability, low cost, environmental friendliness and ease of use. [112]

The ability of 3D printing to break the inherent limitations of battery shape and size and transform Li-ion battery from simple 2D to complex 3D structures are advantages that may be widely used in the fabrication of electrodes for solid Li-ion batteries.

Many 3D printing techniques such as fused deposition modeling (FDM), stereolithography (SLA), and direct ink writing (DIW) have been reported for processing solid-state lithium-ion battery electrodes.[113-115] However, the research on 3D printing of solid electrolytes is very limited. Compared with traditional processes for manufacturing solid electrolytes such as tape casting, 3D printing still has unique advantages.[116] Excellent controllability of geometric shape and high precision of complex structures of 3D printing method have shown compelling advantages in the field of manufacturing solid-state electrolytes.

SSEs can generally be mainly divided into solid polymer electrolytes, inorganic solid electrolytes and composite SSEs. There are significant differences in the mechanical properties of gel polymer electrolytes and ceramic electrolytes. Ceramic materials have a high modulus of elasticity and polymer materials have a low modulus of elasticity. Polymers are also generally easier to process than ceramics, which reduces the overall cost of manufacturing. Ceramics, on the

other hand, are better suited to high temperatures or other harsh conditions than polymers.[117]

2.3.1 Direct Ink Writing

The first to use DIW to print ion liquid gel solid electrolytes was Ho et al. in 2010. After more than 70 cycles, the Li-ion battery with an energy density of 1.2 mWh cm⁻² and the storage capacity of 0.98 mAh cm⁻² was achieved by DIW printing.[118] Li₄Ti₅O₁₂-graphene oxide material was successfully printed by Fu et al. as a polymer composite electrolyte.[119] Combining polymers with nanoceramic Al₂O₃, solid electrolytes with controllable porosity were successfully printed by Blake et al. [120] In 2018, Li₇La₃Zr₂O₁₂ (LLZO) material successfully prepared ceramic electrolytes lithium-ion battery with different micron-scale features by DIW printing (Figure 2.8). This work was reported by McCown et al. [121]

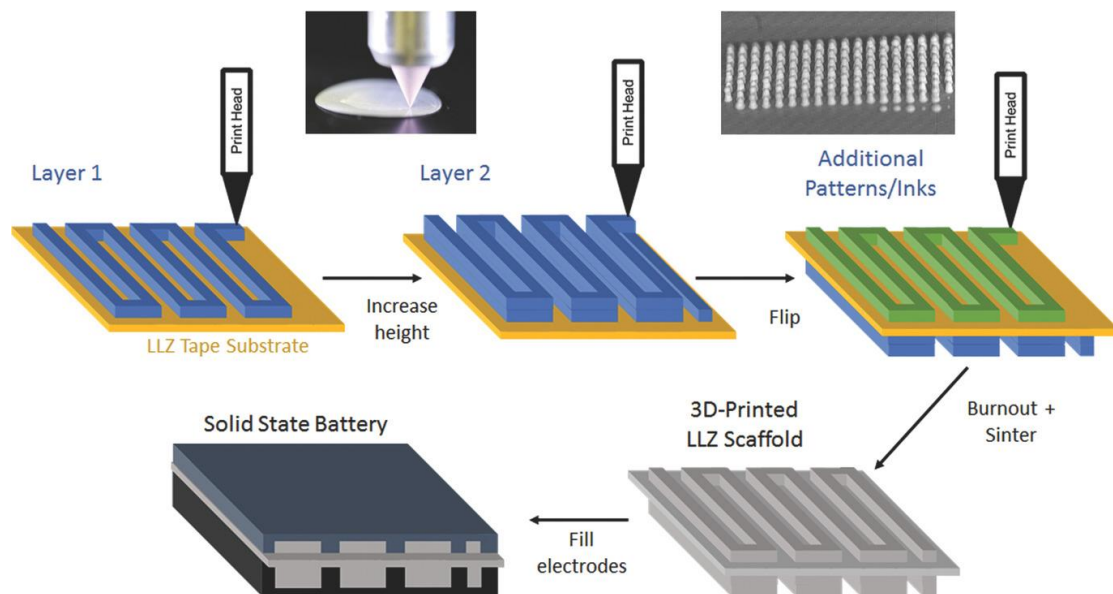


Fig. 2.8 DIW 3D printing scheme of Li₇La₃Zr₂O₁₂ (LLZO) solid electrolyte material.[121]

The preparation of electrolyte structures using the above method enables solid-state lithium-ion batteries with desirable low full-cell resistance, mechanical

properties and increased energy and power densities. The controllability of complex shapes and precision adjustments offered by DIW 3D printing has made it a promising method for fabricating solid electrolytes. However, the full potential of these advantages has to be realized in the design of such structures. Presently, traditional two-dimensional planar structures, such as sandwich and thin disk structures, remain the preferred designs for 3D printing solid electrolytes. Thus, the 3D printing of complex, high-precision, solid-state electrolyte materials using DIW 3D printing presents a new challenge.

To date, there have been no reports on the 3D printing of LLZTO materials. Therefore, this paper aims to address this gap by focusing on the realization of 3D printing of LLZTO using DIW 3D printing technology. By demonstrating the feasibility of 3D printing high-precision LLZTO structures, this study aims to open up new avenues for designing and optimizing solid-state electrolytes, thereby contributing to the development of high performance and safe Li-ion batteries.

2.3.2 Stereolithography

The Stereolithography apparatus (SLA) has gained widespread popularity as a 3D printing technique due to its ability to produce high spatial resolution. It is now being utilized for the production of SSEs using materials such as polymers, ceramics, and glass.[115, 122, 123] By selectively curing resins with ultraviolet light, visible light and NIR (Near Infrared Spectrum) light sources, SLA is able to fabricate complex 3D spatial grid structures. The curing process typically occurs on the surface of the liquid, and as each layer is cured, the platform supporting the printed parts are incrementally raised or lowered.[124] The photocurable resin used in SLA primarily comprises photoactive monomers with a small amount of additives such as photoinitiators. SLA possesses the capability to fabricate intricate three dimensional geometries, including

miscellaneous hollow engraved features with fine resolution up to the micron scale.[125] As a result, it is believed that SLA holds significant potential for fabricating solid-state electrolytes, especially when compared to DIW 3D printing technology, due to its ability to print arbitrary 3D geometries.

Kim SH et al. prepared solid-state polymer electrolyte layers by SLA and then assembled them into poly laminate structured lithium-ion batteries with different form factors in 2015.[126] In 2017, Chen Q. et al. reported a resin based on ultraviolet curable polyethylene glycol and the gel polymer SSE was successfully printed by SLA. The printed zigzag-like shaped electrolyte increased the contact region with the electrodes, resulting in an ion conductivity comparable to that of liquid electrolytes.[127] Zeker et al. developed in 2018 a composite solid electrolyte composed of $\text{Li}_{1.4}\text{Al}_{0.4}\text{Ge}_{1.6}(\text{PO}_4)_3$ ceramic material with polymer (polyepoxides) which were printed by SLA as polymer scaffold, and then the mold was filled by LAGP powder.[128] After sintering, no polymer remains on the ceramic frame. At this time, the polymer is re-infiltrated to fill the pores of the ceramic to obtain a ceramic-polymer composite solid electrolyte.

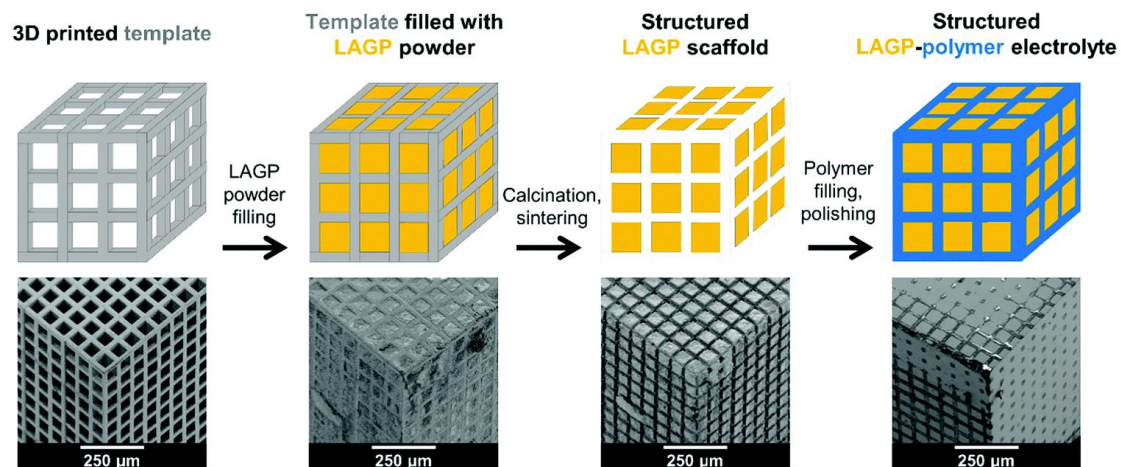


Fig. 2.9 3D printing hybrid electrolyte flow chart and corresponding structural SEM image.[128]

As shown in Fig. 2.9, this processing technology can freely adjust the ratio of

ceramics and polymers, and print high-precision microstructures, such as cubes, helices, diamond and bijel-derived structures. The ion conductivity of the gyroscopic hybrid SSE is $1.6 \times 10^{-4} \text{ S cm}^{-1}$, which is similar to the conductivity of solid-state electrolyte made of LAGP powder, while the printed electrolyte exhibits 27.9% higher compressive strength and 4.9 times higher flexural strength. However, obtaining a ceramic solid electrolyte through SLA is not straight forward. SLA printable photoresins or precursor polymers have limited availability and high cost (approximately \$1000/kg for photoresins and more expensive precursors) and require manual support to print hollow or overhanging structures. This complex and costly SLA process is not suitable for industrial mass production. The low-cost fabrication of solid-state electrolytes by SLA process is still a challenge.

2.3.3 Fused Deposition Modeling

The Fused Deposition Modeling (FDM) technology uses a similar molding mechanism as DIW, both being based on extrusion molding, but differ in terms of raw materials and feeding processes. FDM requires thermoplastic materials in filament form, which are driven by wheels to the extrusion head, where they are softened or melted and then flow through the printing nozzle. The extruded material cools and solidifies after deposition onto the substrate, either through crystallization or cooling below the glass transition temperature of materials. Common thermoplastic materials in FDM are polylactic acid and acrylonitrile-butadiene-styrene. The PLA filaments are gaining popularity as a bioplastic because of their environmental friendliness. While the low ion conductivity limits the applications of thermoplastic materials in the manufacture of solid electrolytes. Hence, the development of printable materials with high ion conductivity is crucial for the production of solid-state electrolytes by FDM. Despite the advantages of FDM, such as precise control over complex shapes, the fabrication of highly filled thermoplastic Li-ion conductive composite

materials remains a challenge.

By injecting a mixture of propylene carbonate, EMC and LiClO₄, Reyes et al. synthesized PLA-based electrolyte material filaments suitable for FDM printing for the first time in 2018.[129] Compared with traditional lithium-ion battery electrolytes, this solid-state electrolyte printed by FDM has a lower coulombic efficiency and a maximum ion conductivity of only 0.031 mS cm⁻¹. [130] FDM has received more and more attention because of its advantages such as low printing cost, printable multi-material structure, and ability to print large sizes. However, the printed samples show poor surface quality and structural controllability when solid electrolytes are printed by FDM. These defects are caused by the filamentous printing material and the low melting temperature of the material, etc.

Chapter 3:

Materials and sample preparation

This chapter is adapted in part, with permission, from the following sources[13, 131].

3.1 Materials

In this section, an overview of the chemicals used in the experiments will be given, including additives to improve rheological properties, different solid particles and solvents.

3.1.1 Particles

The solid particles mainly used in this study are garnet-type inorganic non-metallic powders- $\text{Li}_{6.4}\text{La}_3\text{Zr}_{1.4}\text{Ta}_{0.6}\text{O}_{12}$ (LLZTO). Stearin wax as a secondary solid particle is used to improve the rheological behavior of the paste.

Garnet-type Inorganic solid electrolytes- LLZTO

Due to its oxidation stability, high ion conductivity, thermal stability and suitable price, LLZTO is one of the best options as SSE for Li-ion batteries. In this study, the LLZTO powder (density $\rho = 5.5 \text{ g cm}^{-3}$) is purchased from Ganfeng Lithium Co.,Ltd (Xinyu, China). The powders are produced by a three-step solid-state reaction [132, 133]. Fig 3.1 shows the arbitrary, isometric shape of the particles. From the supplier data, the particle size distribution characteristics of these powders are:

$$X_{10} = 3.5 \mu\text{m}$$

$$X_{50} = 7.2 \mu\text{m}$$

$$X_{90} = 14.5 \mu\text{m}$$

where X_{10} , X_{50} and X_{90} are the diameters at which 10%, 50% and 90% of the sample's volume comprise particles with the diameters less than that value.

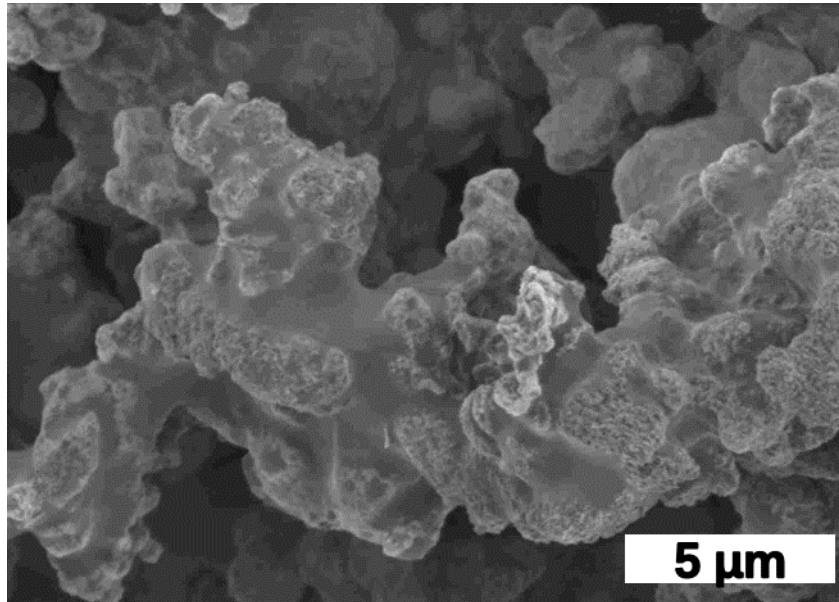


Fig.3.1 Scanning electron microscopy (SEM) image of LLZTO particles.

The X_{10} data is consistent with the laboratory particle size test results (Fig 3.2).

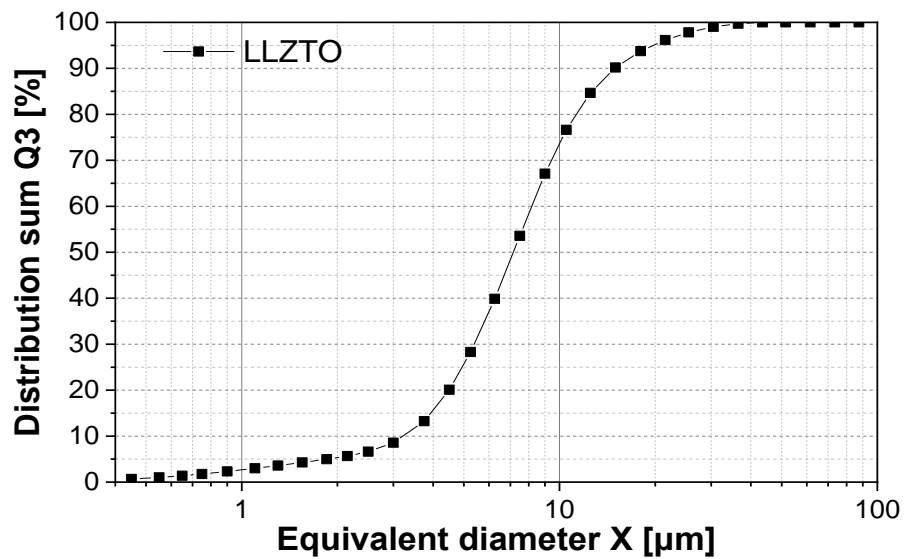


Fig.3.2 Particle size distribution of the LLZTO powder as obtained from Fraunhofer diffraction

Stearin wax

Stearin wax is a mixture of stearic and palmitic acid that is obtained from the triglycerides contained in vegetable and animal fats and oils by saponifying them and then acidifying the soapy water. Stearin wax is purchased from TrendLight Creativ GmbH. The stearin wax density $\rho = 0.921 \text{ g cm}^{-3}$, $X_{50} = 1 \text{ mm}$ and melting temperature $T_m = 70 - 80 \text{ }^\circ\text{C}$.

3.1.2 Additives

As mentioned above, the additives influence the rheological properties of 3D-printable inks. The most commonly used additives include:

- **Secondary phase fluid:** When a small amount of the secondary fluid, immiscible liquid phase is added to the suspension, the rheological properties of the mixture are changed.[134]
- **Dispersant:** Dispersant is a kind of surfactant, which can facilitate separation of particles in the suspension, avoid the particles from settling or agglomerating in the suspension, in order to enable the particles to be stably dispersed in the medium.

Secondary phase fluid

Two different secondary phase fluids have been used for different formulations in this study.

Ethylene glycol ($\geq 99.2\%$, $\rho = 1.11 \text{ g cm}^{-3}$, Merck KGaA, Germany) is an organic compound with the formula $(\text{CH}_2\text{OH})_2$. It is an odorless, colorless, flammable, viscous liquid. Fig 3.3 shows the chemical structure.



Fig. 3.3 The chemical structure of ethylene glycol

N,N-dimethylformamide (DMF, $\geq 99.9\%$, $\rho = 0.95 \text{ g cm}^{-3}$, Sigma–Aldrich) is an organic compound with the formula $(\text{CH}_3)_2\text{NC(O)H}$. Fig 3.1.4 shows the chemical structure.

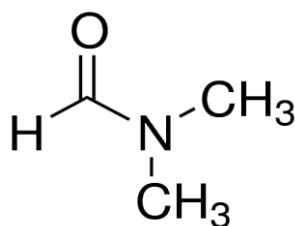


Fig. 3.4 The chemical structure of DMF

Dispersant

Sorbitan monooleate (Span 80) is a sorbitan fatty acid ester, an ester of sorbitol or 1,4-sorbitan anhydride (sorbitan for short) with a fatty acid, mainly palmitic acid, linoleic acid and oleic acid. Span 80 is purchased from Merck Schuchardt OHG, Germany, $\rho = 0.99 \text{ g cm}^{-3}$ and HLB = 4.2, is added to the samples to control the microstructure and hence flow behavior. The dispersant was used without further treatment.

3.1.3 Solvents

Solvents are necessary to convert solid particles into the paste.

Polydimethylsiloxane

Polydimethylsiloxane (PDMS) is a silicon-containing high molecular polymer. It

is odorless and highly transparent. With different relative molecular weight, the PDMS has different appearance, ranging from a very high viscosity liquid or silica gel to a colorless transparent liquid. PDMS has the characteristics of heat resistance, cold resistance, small change in viscosity with temperature, water resistance, and low surface tension. In this study, PDMS with the following specifications: molecular weight $M_w = 17100 \text{ g mol}^{-1}$, dynamic viscosity $\eta = 490 \text{ mPa s}$, density $\rho = 0.966 \text{ g cm}^{-3}$, is purchased from ABCR GmbH, Germany. Fig 3.5 shows the chemical structure. The PDMS Industrial synthesis is prepared using dimethylchlorosilane and H_2O by the following reaction:

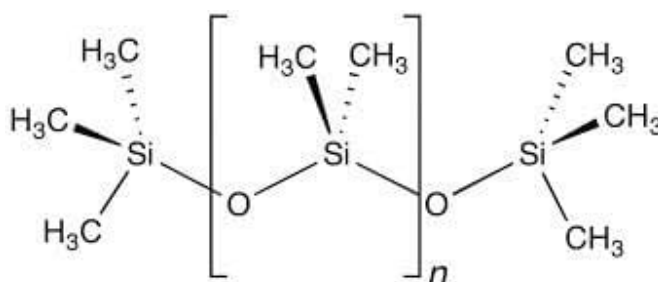
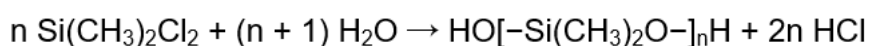


Fig. 3.5 The chemical structure of PDMS

Paraffin oil

Paraffin oil is an oily liquid. It is transparent, odorless and colorless. Fractionated from petroleum crude oil, usually composed of saturated hydrocarbons. The high viscosity paraffin oil with viscosity $\eta = 110 - 250 \text{ mPa s}$ and density $\rho = 0.865 \text{ g cm}^{-3}$ was purchased from Carl Roth GmbH & Co. KGaA, Germany. .

Castor oil

Castor oil is extracted from castor bean seeds, which is a type of vegetable oil. The composition of castor oil is: 81% to 86% ricinoleic acid, 6% oleic acid, 2%

stearic acid, 3% palmitic acid and 4% linoleic acid.[135] It has a distinct taste and odor and is a colorless or light yellow liquid. Its density is 0.961 g cm^{-3} . The other significant components are oleic acid and linoleic acid. The castor oil is purchased from Fisher Scientific U.K. Limited.

3.2 Ink preparation

3.2.1 Speed mixer

The speed mixer (Hauschild GmbH, Hamm, Germany) uses the dual asymmetric centrifuge [136]. Unlike traditional centrifugal mixers, the speed mixer provides additional rotation of the samples around its own vertical axis. The sample material is constantly moved towards the center of the centrifuge by the additional rotation, whereas traditional centrifugal mixers can only force the sample material continuously to the outside. When the two counter-rotating movements are combined, a unique shear force is created to effectively homogenize the sample. The device DAC 150.1FVZ has been used in this study (see Fig. 3.6). Suspensions were prepared by mixing LLZTO particles into the bulk phase in the speed mixer. A sample volume of 1-5 mL in 25 mL cups was mixed for 1 min at 3000 rpm. Subsequently, the secondary fluid or non-ionic wetting agent was added and the suspension was mixed for 2 min at 3000 rpm. Finally, the paste ink is produced.



Fig 3.6 SpeedMixer™ DAC 150.1FVZ

3.2.2 Three roll mill

After preparation in the speed mixer samples still included some agglomerations. Breaking a number of aggregates between the solid particles and obtaining the well dispersed uniform paste became the key to the preparation of the ink. To break aggregates in the ink, external shear is efficient and direct. The three roll mill is a common type of device for preparing agglomerate-free pastes. In this thesis, the machine EXAKT E80 has been used (see Fig. 3.7).



Fig. 3.7 Three roll mill EXAKT E80

The working principle of the three roll mill grinding machine is: the solid particles are pressed against each other by the surfaces of the three horizontal rollers and rubbed at different speeds to finally achieve particle grinding. Here, the speeds of the three rollers from left to right are respectively marked as V_1 , V_2 , V_3 , and $V_1 < V_2 < V_3$. The particles are placed between the left roller and the middle roller (see Fig. 3.8). Friction between the rotating roller and the sample creates shear forces on the particles. Because of the different speeds between the two different rollers, the shear forces increase from the slower roller to the faster roller. Different shear forces acting on the same agglomerate cause the agglomerated particles to separate.

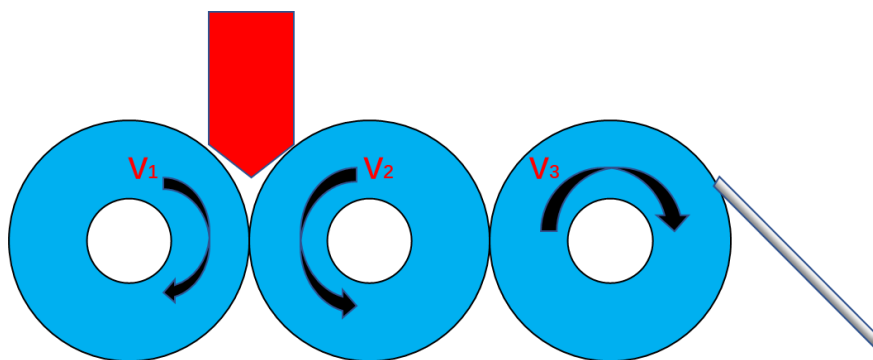


Fig 3.8 Process of three roll mill

In addition to the speed of the rollers, the gap between the two rollers will also affect the strength of the shear force. The gap set between the rollers limits the maximum diameter particles that can pass through. Some solid state particles are soft and deformable. Hence, it is equally significant to gradually reduce the gap size. Otherwise, the solid particles may lose their original shape, e.g. change from spherical to flake-like. Changes in shape can affect the rheological properties of the prepared inks.

In this study, the samples are milled seven times and the detailed parameters are shown in Table 3.2.1. The first gap is the separation between the left roller and mid roller. The second gap is the separation between the mid roller and right roller. The rotational speed of the 3 rollers is set by the manufacturer to be 1:3:9. The angular velocity of the right roll is constant value: 150 rpm.

Table 3.2.1 Parameters for the 3 roll mill process. The angular velocity of the right roller is constant value: 150 rpm.

Round	1st Gap (μm)	2nd Gap (μm)
1	60	50
2	50	40
3	40	30
4	30	20
5	20	10
6	10	5
7	5	5

Finally, ink preparation using the high-speed mixer and further homogenization by the above-mentioned three-roll mill grinding step successfully breaks up the LLZTO particle aggregates to produce inks suitable for 3D printing.

3.3 Formulations

The details of different inks are shown in Table 3.3.1. The solid phase contents of suspensions with different bulk phase were $\phi_{\text{solid-PDMS}} = 35 \text{ vol\%}$ and $\phi_{\text{solid-}}$

Paraffin oil = 39 vol%, respectively. The ratio of secondary phase to solid phase was $\varphi_{\text{sec}}/\varphi_{\text{solid}} = 0.171$ for capillary suspensions when the PDMS is bulk phase and $\varphi_{\text{sec}}/\varphi_{\text{solid}} = 0.103$ for capillary suspensions when the paraffin oil is bulk phase.

Table 3.3.1 Composition of the three inks used for printing.

Ink	1		2		3	
Solid phase (vol%)	LLZTO	26	LLZTO	26	LLZTO	40
Bulk phase (vol%)	PDMS	59	Paraffin oil	57	Castor oil	54
Second phase /dispersant (vol%)	Ethylene glycol	6	DMF	4	Span80	6
Stearin wax (vol%)		9		13		--

The castor oil-based ink formulation is shown in Table 3.3.1. The ink does not contain stearin wax and $\varphi_{\text{solid LLZTO}} = 40$ vol%.

Chapter 4:

Methodology

This chapter is adapted in part, with permission, from the following sources[13, 131, 137-140]

4.1 Contact angle

The three-phase contact angle of the secondary fluid on the LLZTO within the primary phase was measured using a static drop tensiometer (SCA 20, DataPhysics Instruments GmbH, Filderstadt, Germany). The LLZTO solid powder was compressed into a thin disc shape (25.5 mm in diameter, 7 mm in thickness) using a hand press and immersed in paraffin oil or PDMS substrate. A droplet of the secondary fluid was squeezed from a needle (1.2 mm diameter) and settled on the LLZTO disc. The observed droplets are shown in Fig. 4.1.1. The droplet shape was recorded by the equipped camera, and the three-phase contact angle was obtained by Drop Shape Analysis (DSA).

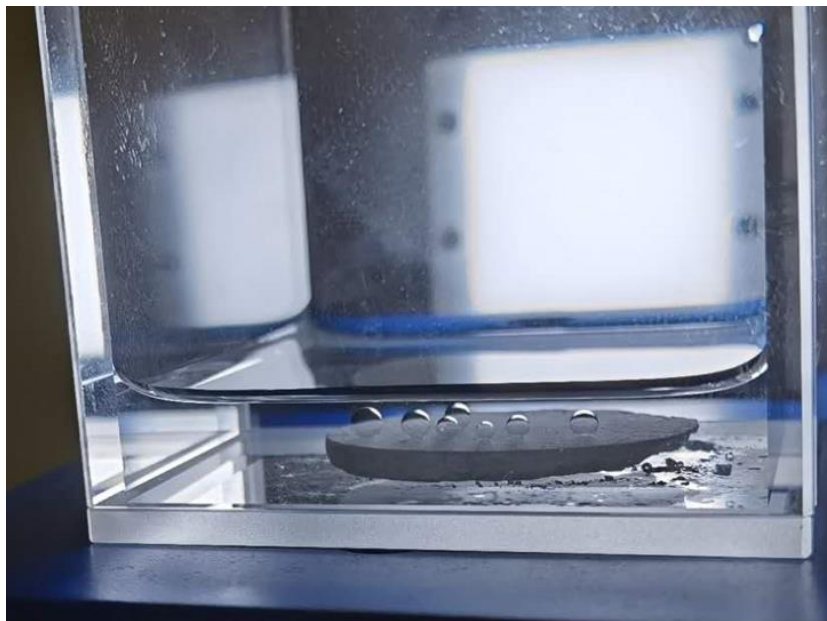


Fig. 4.1.1 Three-phase contact angle

4.2 Rheological measurements

The rheological properties of AM inks are very important for the printing process. Therefore, the rheological properties of the ink must be measured. In this section, the measurement methods for the different rheological properties of the inks in this study, including yield stress, viscosity, shear modulus, and slip velocity, are described. All rheological experiments were performed at room temperature.

4.2.1 Yield stress measurement

The minimum stress required to force the slurry to flow is the apparent yield stress σ_y . High solid pastes often exhibit wall slip effects when measured using conventional plate-plate, cylinder geometries and cone-plate. Hence, yield stress measurements were performed using a stress-controlled rotational rheometer (Physica, MCR 501, Anton Paar GmbH, Germany) setup equipped with a vane-and-cup fixture.[141]. It only considers shear stress, not viscous flow using the vane geometry in the cup, and slip at the wall can generally be neglected.

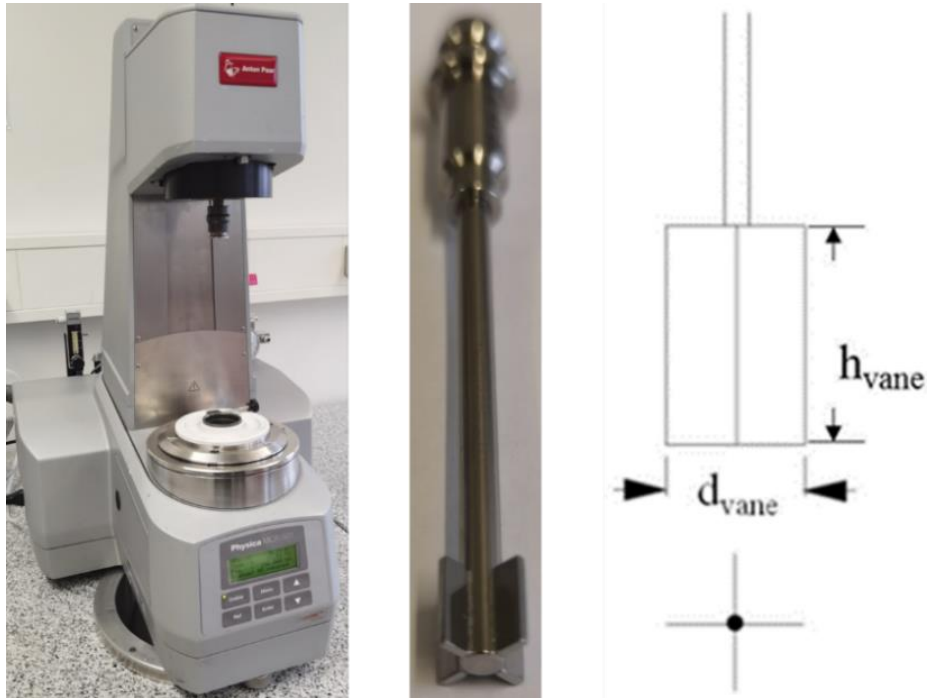


Fig 4.2.1 MCR 501 Physica and vane used for yield stress measurement in this study

The vane geometry used in this thesis has a diameter of $d_{\text{vane}} = 5 \text{ mm}$ with 4 blades, and all the four blades have a height of $h_{\text{vane}} = 8.8 \text{ mm}$ (See Fig. 4.2.1). The cup in MCR 501 has a diameter of $d_{\text{cup}} = 10 \text{ mm}$.

Measurements were conducted applying a stepwise controlled stress mode, varying the stress from 10 to 10^4 Pa in 31 steps equally separated on a logarithmic scale, while each stress was applied for 30 s. The yield stress was defined as the stress at which the sample begins to flow irreversibly and here it was determined from deformation vs shear stress data using the tangent intersection point method.[141] [142] The critical stress at which the tangents applied to the linear and flow region of the stress-dependent deformation curve cross is defined as σ_y (Fig. 4.2.2). All rheological measurements were performed at 20 °C. For the same sample, after three measurements, the standard deviation was calculated.

Elastic deformation occurs only when the stress is below the yield stress, so

the first range should theoretically have a slope of 1. If a value slightly above 1 is found in multiple empirical trials. There may be irreversible structural changes below the apparent yield stress.

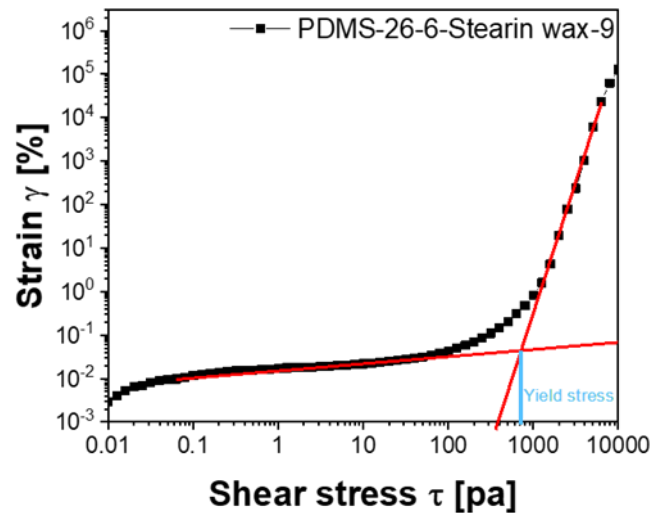


Fig. 4.2.2 The yield stress was determined from deformation vs shear stress data using the tangent intersection point method.

4.2.2 Viscosity

Measurements of flow curves are typically performed using a rotational rheometer (MCR 501, Anton Paar) with a plate-plate geometry (25 mm diameter) and a gap size of 0.5 mm. Viscosity is a function of shear rate, and their functional relationship is reflected in the flow curve. The plate-plate geometry is shown in Figure 4.2.3. The gap dimension between the upper plate (of diameter R) and the bottom plate is h. The upper plate is rotated around the axis by applying a torque T, which is performed in the shear stress control mode. The shear stress is related to the applied torque, the shear stress for plate-plate geometry is given by:

$$\sigma = \frac{2T}{\pi R^3} \quad (1)$$

The angular frequency ω is known by device detection. It is assumed that there is a uniform shear inside the sample and the gap is completely filled by the sample during the experiment. It is also assumed that no slip occurs between the rheometer wall and the sample. The viscosity η is defined as:

$$\eta = \frac{\sigma}{\dot{\gamma}} \quad (2)$$

The torque T is given by:

$$T = \frac{2\pi R^3}{\dot{\gamma}^3} \int_0^{\dot{\gamma}R} \gamma^2 \sigma(\dot{\gamma}) d\dot{\gamma} \quad (3)$$

and the shear stress is given by:

$$\sigma_R = \frac{\sigma_{R,S}}{4} \left(3 + \frac{d \ln \sigma_{R,S}}{d \ln \dot{\gamma}R} \right) \quad (4)$$

and the shear rate is given by:

$$\dot{\gamma}_R = \frac{\dot{\gamma}_a}{4} \left(3 + \frac{d \ln \dot{\gamma}_a}{d \ln \sigma_R} \right) \quad (5)$$

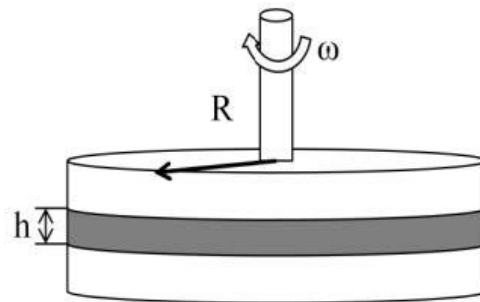


Fig 4.2.3 Schematic diagram of a plate-plate setup of a rotational rheometer with the gap height h and radius R .

However, this method is not sufficient to characterize the inks designed in this study. A capillary rheometer has to be used to obtain the viscosity at process-

relevant shear rates [143]. At a controlled volumetric flow rate, the sample is forced through a capillary tube with a diameter of 0.5 mm and a length of 80 mm at a shear rate range up to 20000 s^{-1} . The resulting extrusion pressure was recorded using a pressure sensor (pressure range from 0 to 1,000 bar, American Industrial Sensors) and the measured pressure is proportional to the shear viscosity of the fluid. [144]. A schematic drawing of the capillary rheometer is shown in Fig. 4.2.4.

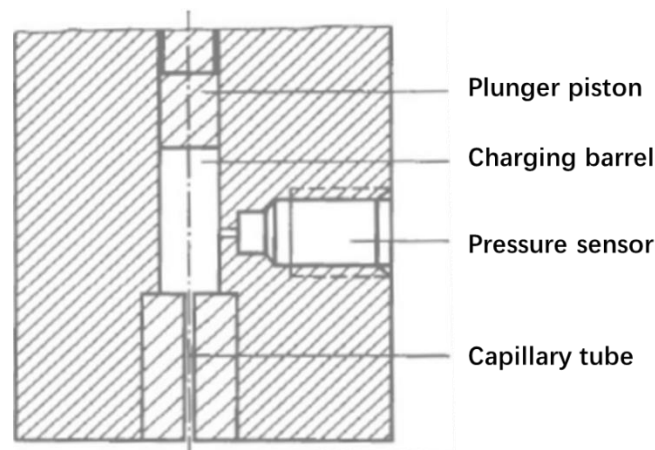


Fig 4.2.4 The structure of the capillary rheometer

4.2.3 Modulus

Small-amplitude oscillatory shear experiments were performed on all designed inks using a rotational rheometer (Physica, MCR 501, Anton Paar GmbH, Germany) equipped with a plate-plate geometry (diameter $D = 25 \text{ mm}$). Both plates used in the experiments were roughened (sandblasted surface) to prevent wall slippage, and the gap distance was chosen between 0.5 mm and 2 mm. Small-amplitude oscillatory shear experiments cover the frequency range from 0.1 to 100 rad s^{-1} and are tested at strain amplitudes small enough ($\gamma \leq 0.01\%$) to provide a linear material response.

4.2.4 Slip velocity

Slip velocity measurements were conducted using a rotational rheometer (Physica, MCR 501, Anton Paar GmbH, Germany) with the plate-plate geometry (25 mm diameter) and gap size of 2 mm as described in Xu et al.[145] Measurements were carried out at selected shear stresses between 400 Pa and 1,000 Pa and a total measuring time of 300 s. The slip velocity $v = 2\pi nR$ at the rim of the plate is given by the rotation speed n and the plate radius R .

4.3 3D printing

4.3.1 Direct Ink Writing (DIW)

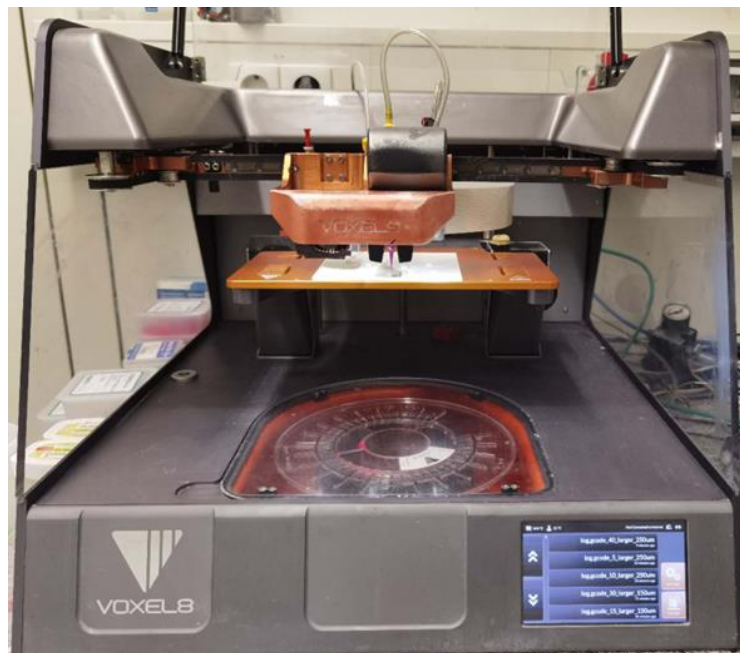


Fig 4.3.1 Voxel8 3D Electronics Printer for DIW

In this study, the Voxel8 3D Electronics Printer shown in Fig. 4.3.1 was used. The inks were extruded through polyethylene tapered nozzles (inner diameters of: 150 μm , 200 μm , 250 μm and 400 μm ; Nordson EFD). A syringe pump (PHD Ultra; Harvard Apparatus) was mounted on a 3D positioning station (ABG

10000; Aerotech Inc.) for extruding the inks at a constant volumetric flow rate. 10 mL syringes (Luer-Solo; ALMO-B. Braun company) were loaded with the ink and installed on the syringe pump. The ink was filled into the syringe with a spatula carefully avoiding the entrainment of air bubbles. By programming the translation of the console in the x-y-z direction and setting the parameters of the air pump, the syringe pump can print with controlled translation velocity and pressure. The chosen printing parameters are shown in Table 4.3.1.

Table 4.3.1 Printing parameters for different ink compositions and nozzle diameters.

Composition	Nozzle diameter	Translation velocity	Pressure
PDMS	150 μm	200 mm/s	8 MPa (Max)
Paraffin	150 μm	100 mm/s	8 MPa (Max)
Castor	150 μm	400 mm/s	7.5 MPa

4.3.2 Stereo lithography apparatus (SLA)

Stereolithography Apparatus (SLA) is the AM process that uses visible light, NIR (Near Infrared Spectrum) light and ultraviolet (UV) lasers to transform photosensitive resin (a liquid material that hardens when exposed to ultraviolet light) into a solid 3D object layer by layer. Cooperating with Lithoz company and using their CeraFab 7500 3D printer, it was attempted to create three-dimensional complex scaffolds by printing specially made inks containing LLZTO powder and a tailored photo-sensitive reactive binder. Figure 4.3.2 shows the Lithoz company CeraFab 7500 3D printer for SLA.



Fig 4.3.2 Lithoz company CeraFab 7500 3D printer for SLA

4.3.3 Fused deposition modeling (FDM)

Fused deposition modeling (FDM) is the AM process by extruding material. FDM uses thermoplastic materials in the form of filaments to build parts layer by layer, enabling selective deposition of molten material in predetermined paths. A multifunctional 3D printer for FDM is shown in Figure 4.3.3. FDM feeds molten filamentous material through a heated nozzle. The molten filaments are deposited layer by layer onto a horizontal platform to build a complete part. By using digital design or other design methods, the designed structure is converted to physical size by the 3D printing machine itself. After the 3D printer receives the instruction, it heats up the temperature of the nozzle. When the nozzle is raised to a preset temperature, thermoplastic filaments are fed into the nozzle through an extrusion head connected by a three-axis system. This system enables the extruded filaments to move freely in three dimensions. The material is melted through a heated nozzle and then extruded into filaments,

depositing one layer along the designed path and continuing to deposit the next layer. After the designed structure is fully deposited, the material is completely cooled and solidified on the platform. Post-print part cooling can be accelerated through physical methods such as installing fans on the extrusion head.

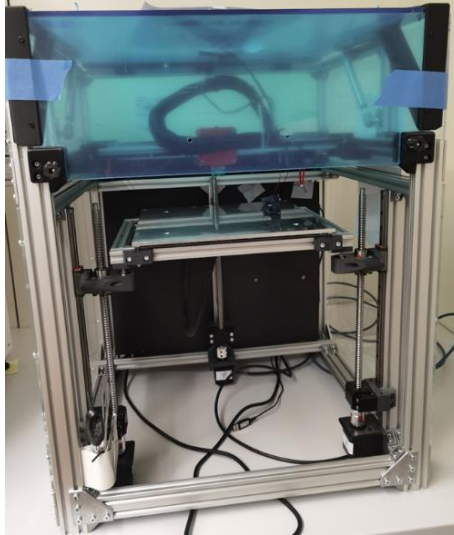


Fig 4.3.3 Multifunctional 3D printer for FDM

4.4 Sintering

The capillary suspension-based inks were printed on commercial aluminum oxide ceramic plates (120 x 120 mm, Al₂O₃ content: 99.5%, Keramische Folien GmbH & Co. KG). Square, triangular, and hexagonal honeycomb lattices were 3D printed with 20 layers with the sample size of 5.7 × 5.7 × 3 mm. The square structure was an excellent test structure for evaluating the printing behavior of the ink, as it consists of many spanning bridges that can collapse or break if the storage modulus of the ink is too low. After preliminary trials with 400 μm, 250 μm and 200 μm nozzles, all structures were printed with nozzle diameters of 150 μm.

Organic components in the green bodies were burned out in a debinding furnace (LVT 05/11, Nabertherm GmbH, Germany). For this, the samples were heated from 25 °C to 300 °C at a rate of 1 °C min⁻¹ and subsequently, the

temperature was held constant for 1 h at 300 °C. Afterwards, the temperature was increased to 800 °C at a heating rate of 1 °C min⁻¹ and was held for 5 h at 800 °C. Finally, the oven was cooled down to 400 °C at a cooling rate of 2 °C min⁻¹. After 5 min at a constant temperature of 400 °C, the oven was further cooled down to room temperature without temperature regulation.

A high temperature furnace (LVT 05/11, Nabertherm GmbH, Germany) was used to sinter the samples between 900 °C and 1100 °C. The furnace was heated up to the sintering temperature at 1 °C min⁻¹. The final temperature was held constant for 15 h. Subsequently, the furnace cooled down to room temperature at 2 °C min⁻¹.

4.5 Structural Characterization

Scanning-electron-microscopy (SEM) (S-4500; Hitachi High-Technologies Europe GmbH) images of the surface and of the crosscut of sintered parts were used to analyze their microstructure. To prepare appropriate cross sections of sintered parts, epoxy resin was infiltrated, and subsequently cured at 70 °C for 20 h. Finally, the specimens were grinded and polished. The filament diameter size and surface topography of the cellular ceramics were analyzed using a digital microscope (VHX-950 F, KEYENCE Germany GmbH).

The printing experiments discussed here result in cellular structures with filaments or struts of high internal porosity. The strut porosity ε_s was determined using Archimedes' principle according to DIN EN 993-1. The overall density of the printed cellular structures was determined from the structures' volume and weight. The true porosity ε^* (see Table 6 below) was calculated from the structure's density and ceramic material density.

The crystal structures of LLZTO powder and unsintered powder at different sintering temperatures were studied by X-ray diffraction (XRD). For the patterns

the scattering angle range 2θ was scanned from 15° to 78° in steps of 0.01° with a measurement time of 0.2 s per step (D8 advance, Bruker, USA). The elemental composition was investigated by energy-dispersive X-ray spectroscopy (EDS, Quantax 400 SDD, Bruker, USA).

4.6 Mechanical Measurements

Compressive strength tests of printed and sintered cellular structures were performed using a universal testing machine TA.XT. plus (Stable Micro Systems, UK) equipped with a 10 kN load cell. The samples were polished to obtain a fully flat surface prior to loading and then tested in a displacement controlled mode at a rate of 0.1 mm s^{-1} until failure occurred.

Chapter 5:

Results and discussion

5.1 DIW 3D printing LLZTO

5.1.1 Capillary suspension

Capillary suspensions are ternary fluid/solid/fluid systems. The secondary fluid is immiscible with the bulk phase, and the three-phase contact angles of the two capillary suspension inks were measured using the static drop method as described above [146-148]. As shown in Fig. 5.1.1a, the measured three-phase contact angle of DMF on LLZTO particles is $\theta_{\text{LLZTO-Paraffin oil-DMF}} = 151 \pm 1^\circ$, higher than 90° , the whole system is in the so-called capillary state at this time. Fig. 5.1.1b shows the ethylene glycol-PDMS system, the measured three-phase contact angle is $\theta_{\text{LLZTO-PDMS-EG}} = 137 \pm 3^\circ$, and the system at this time is also in the so-called capillary state. The interfacial tension of the PDMS with ethylene glycol is $\Gamma_{\text{EG-PDMS}} = 17.2 \pm 0.5 \text{ mN m}^{-1}$, the interfacial tension of the Paraffin oil with DMF is $\Gamma_{\text{DMF-Paraffin oil}} = 4.9 \pm 0.2 \text{ mN m}^{-1}$.

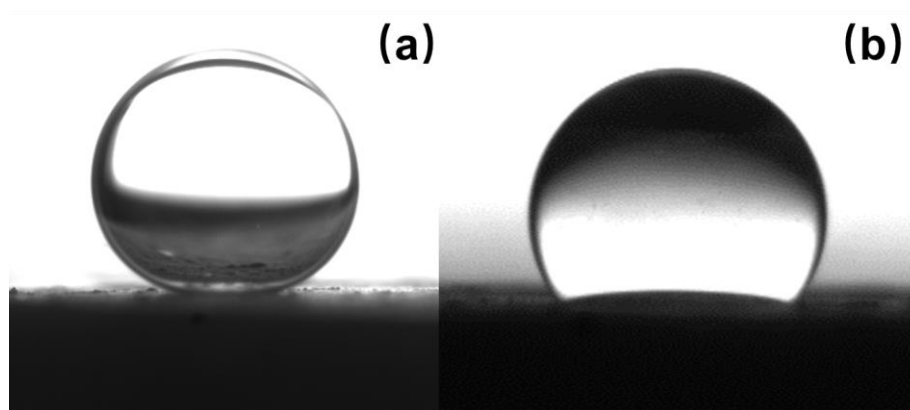


Fig. 5.1.1 Three-phase contact angle (a) DMF on LLZTO particles in paraffin oil; (b) Ethylene glycol on LLZTO particles in PDMS.

5.1.2 Rheological properties of DIW inks

The rheological properties of the inks are an integral and important factor for the 3D printing process. In this section, the influence of rheological properties such as yield stress, viscosity, modulus and wall slip on ink printability will be analyzed in detail.

5.1.2.1 Yield stress

The self-supporting behavior of the ink prevents the shape from collapsing after printing, and it is also crucial that the ink has sufficient yield stress after being squeezed through the nozzle to prevent deformation due to gravity. Therefore, in order to meet the needs of DIW 3D printing, a study on the yield stress of the inks of the two systems described in section 3.3.1 was conducted.

Capillary suspension inks

Two inks were designed using the capillary suspension concept, they are PDMS-based ink and paraffin oil-based ink (see Table 3.3.1). Capillary suspension inks are characterized by changing the rheological properties of the system through capillary forces. Both paraffin oil-based and PDMS-based inks exhibited strong gel-like properties due to the addition of secondary phase fluids, which at this point played a key role in providing sufficient yield strength for the inks. Fig. 5.1.2.1 shows the different textures of the PDMS-based binary suspension and the corresponding capillary suspension, Ethylene glycol is used as the second phase fluid for PDMS-based inks. The self-supporting behavior of the capillary suspension type inks prevents shape collapse and is thus indicated for DIW-type 3D printing in order to prevent the deformation of the printed filaments due to gravity.



Fig.5.1.2.1 Droplets of the suspension based on LLZTO particles and PDMS as bulk phase (left), and with ethylene glycol as second fluid phase (right).

The yield stress σ_y was determined from the deformation and shear stress data by the tangent intersection method. Corresponding data are shown in Figure 5.1.2.2. The red dots in this figure are the yield stress data of PDMS-based inks. The yield stress of the capillary suspension ink increases significantly with the increase of the secondary fluid content, and is more than two orders of magnitude higher than that of the corresponding binary suspension. The yield stress of the PDMS-based ink is $\sigma_{y \text{ PDMS-6}} = 388 \pm 19 \text{ Pa}$ at $\varphi_{\text{sec}} = 6 \text{ vol\%}$. The corresponding binary suspensions exhibits $\sigma_{y \text{ PDMS-0}} = 2 \pm 1 \text{ Pa}$. According to observations and experiments, when the yield stress is greater than 100 Pa, the ink gradually shows its self-supporting characteristics, and the printability of the ink gradually increases with the increase of the volume percentage of the secondary phase fluid. However, when the yield stress is greater than 10000 Pa it is difficult to print well due to the limitations of the air pump pressure of the 3D printer used here. Therefore, the formula ink with $\varphi_{\text{sec}} = 6 \text{ vol\%}$ is selected for 3D printing.

Inks based on paraffin oil showed similar results. The black dots shown in Fig. 5.1.2.2 represent the yield stress of paraffin oil-based ink. When the secondary phase fluid DMF is added to the system, the yield stress of the system increases sharply. At $\varphi_{\text{sec}} = 0 \text{ vol\%}$, the yield stress of the paraffin-based ink is $\sigma_{y \text{ Paraffin-0}}$

= 116 ± 8 Pa. As the volume fraction of DMF increases, the yield stress also increases. At $\varphi_{\text{sec}} = 4$ vol%, the yield stress of the ink reaches $\sigma_{y \text{ Paraffin-4}} = 1172 \pm 60$ Pa. Finally, the ink formulation at $\varphi_{\text{sec}} = 4$ vol% was selected for printing based on these experimental data.

However, the effect of adding secondary fluids is quite different for the two systems. In the absence of the secondary fluid addition, the PDMS-based inks apparently exhibit only weak flocculation and very low yield stress. The addition of secondary fluids results in a strong particle network due to capillary forces and its strength strongly increases with increasing secondary fluid content [149]. The paraffin oil-based system exhibits a maximum yield stress $\sigma_{y \text{ Paraffin-2}} = 1375 \pm 19$ Pa at $\varphi_{\text{sec}} = 2$ vol%, with a slight decrease in σ_y after further addition of secondary fluid. This is commonly observed in capillary suspensions in the pendular state and has been attributed to spherical agglomeration. [150] The systems investigated here are in the capillary state, e.g. particle clusters containing secondary fluid droplets are the building blocks of the percolating particle network. At the high three-phase contact angle of this system ($\theta_{\text{SBS}} = 151 \pm 1^\circ$), the cluster structure changes strongly with the volume of the secondary fluid droplet, and this change in structure is thought to be responsible for the slight decrease in σ_y for the paraffin oil-based system. When stearin wax was added to the system, the yield stress increased by a factor of 2-3 (see Fig. 5.1.2.2 filled symbols), reaching values of $\sigma_{y \text{ PDMS+SW}} = 855 \pm 56$ Pa and $\sigma_{y \text{ Paraffin+SW}} = 3114 \pm 133$ Pa, respectively. For both systems, we attribute this to the increased solids content.

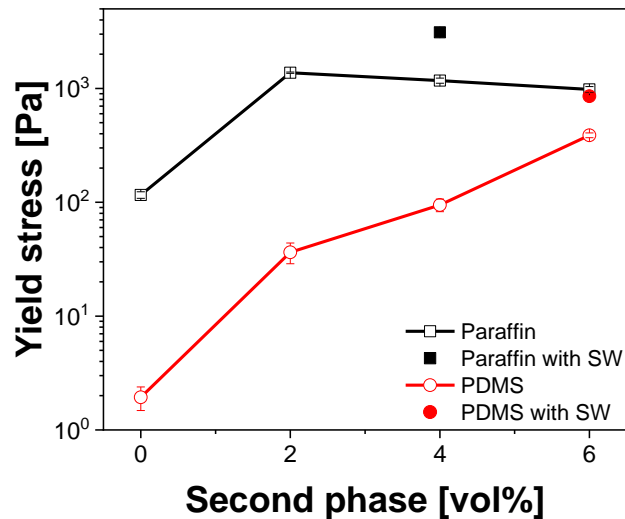


Fig.5.1.2.2 The yield stress σ_y of inks based on paraffin oil and PDMS, the solid dots are the final ink after adding stearin wax.

Dispersant ink

Span 80 is used as a dispersant for castor oil-based ink, and its main function is to promote the separation of LLZTO particles in the suspension. By reducing the interfacial energy between the dispersed particles and the medium, thereby avoid the occurrence of sedimentation or agglomeration, and ensure the stable dispersion of LLZTO particles in the main phase castor oil. Fig. 5.1.2.3 shows the state of the ink before and after the addition of the dispersant, the ink without the dispersant (left) exhibits a harder texture than the ink with the addition of the dispersant (right).



Fig.5.1.2.3 Droplets of the suspension based on LLZTO particles and castor oil as bulk phase (left), and with non-ionic surfactant Span 80 (right).

As shown in Fig. 5.1.2.4, the yield stress increases with increasing $\phi_{\text{dispersant}}$, reaching a value of $\sigma_{y \text{ castor}} = 862 \pm 48 \text{ Pa}$ when adding $\phi_{\text{sec}} = 6 \text{ vol\% Span 80}$. Note that the yield stress values obtained from the creep experiments agree well with the stress amplitudes at $G' = G''$ in the oscillatory stress sweep experiments (Fig. 5.1.3.4.), as previously reported for other particulate gels.[151]

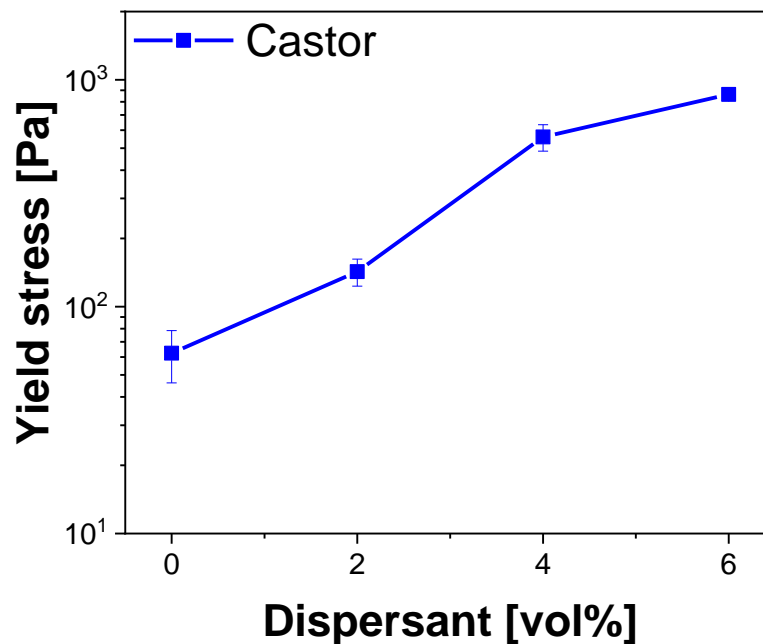


Fig.5.1.2.4 The yield stress σ_y of inks based on castor oil.

5.1.2.2 Modulus of inks

Capillary suspension inks

All three designed inks are highly elastic ($G' > G''$) and the modulus is frequency independent ($\omega = 0.1-100 \text{ rad/s}$) over the entire studied frequency range. The linear viscoelastic energy storage and loss moduli of the samples were all determined by small-amplitude oscillatory shear experimental measurements. The storage modulus of the ink is directly related to the span achievable in direct ink writing, the span being the gap that the printed filament can bridge without deforming or breaking, this will be discussed in the section of 5.1.3.2 in

more detail. Fig.5.1.2.5 shows the energy storage modulus G' for paraffin oil-based and PDMS-based suspensions with different secondary fluid volume fractions. For both systems, the addition of secondary fluids results in a shift from weak to strong gels. The energy storage modulus increases monotonically with the volume fraction of the secondary fluid, resulting in an increase of nearly two orders of magnitude at $\varphi_{\text{sec}} = 6$ vol% addition. The absolute value of the storage modulus is higher for the paraffin oil-based system due to the higher solids content. However, a slightly different dependence on capillary forces was observed for PDMS-based inks compared to paraffinic oil-based inks, as the PDMS-based ink storage modulus increased with increasing secondary fluid content due to capillary forces. In contrast, the storage modulus of paraffinic oil-based inks is less affected by the increase in secondary fluid content because of the lower interfacial tension between the main phase and the secondary fluid and the larger three-phase contact angle.[152] The addition of stearin wax, which acts as a soft filler, has a total of two effects: First, the addition of stearin wax corresponds to an increase in φ_{solid} , since the stearin wax is insoluble in silicone and paraffin oil, so G' increases, as shown in Fig. 5.1.2.5 (solid symbols). This is especially important for PDMS-based inks with their low G' values. However, when stearin wax is added to the ink, the energy storage modulus of PDMS-based inks exceeds 10^5 Pa, which is decisive to minimize the deformation of the filament due to gravity. This is particularly important for demonstrating the lattice structure of free-span filaments. Secondly, the added stearin wax also acts as a lubricant (this will be discussed in Section 5.1.2.3 below).

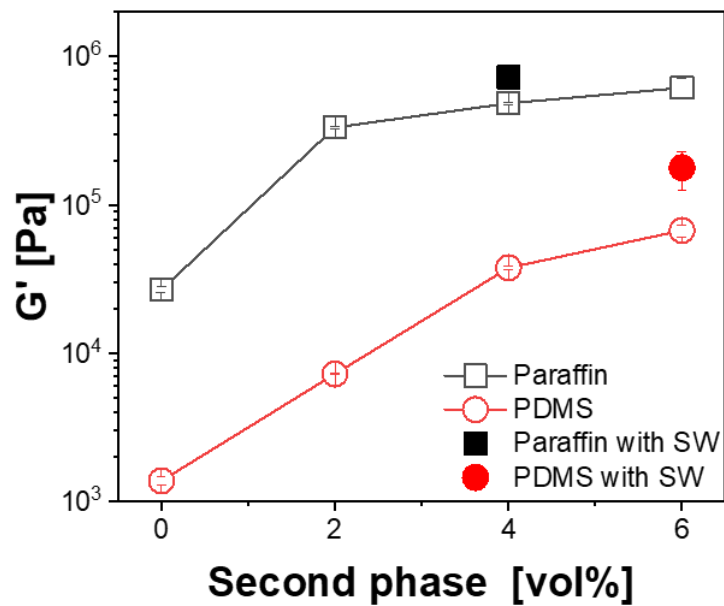


Fig.5.1.2.5 The storage moduli G' of inks based on paraffin oil and PDMS, the solid dots are the final ink after adding stearin wax.

Dispersant ink

The effect of adding dispersant Span80 on the gel strength of castor oil-based LLZTO ink is shown in Fig. 5.1.2.6. The storage modulus decreases monotonically with increasing dispersant content.

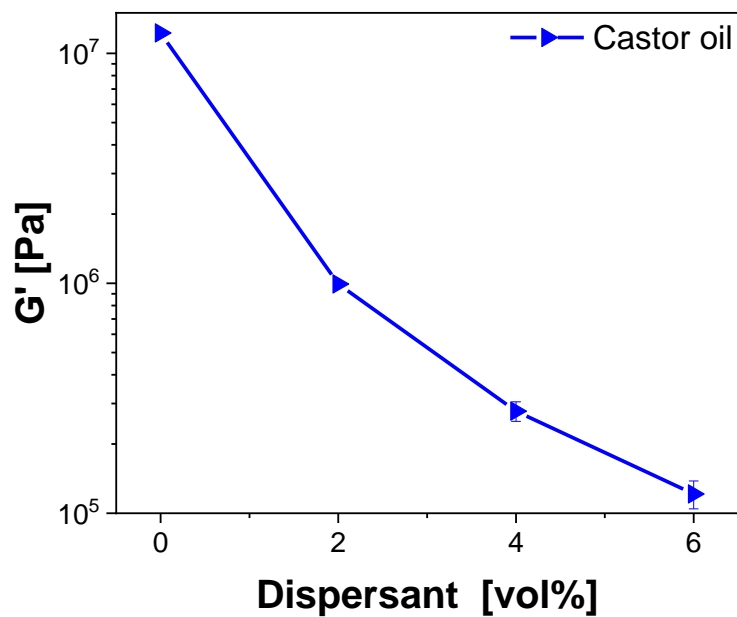


Fig.5.1.2.6 The storage moduli G' of inks based on castor oil.

Furthermore, stress amplitude sweep experiments (Fig. 5.1.2.7) show that the addition of dispersants not only leads to a decrease in the modulus, but also an extension of the linear response range. Due to the high storage modulus ($G' \approx 10^7$ Pa) of inks without dispersants, castor oil-based inks were difficult to extrude from the nozzles and could not be printed even at the maximum pressure (≈ 8 MPa) of the DIW printer. The ink formulation with $\phi_{\text{dispersant}} = 6$ vol% was selected through printing test, and the corresponding storage modulus of the ink at this time was $G'_{\text{Castor}} = 1.2 \pm 0.2 \times 10^5$ Pa, which fully met the requirements of DIW-type 3D printing. Note that the yield stress values obtained from the creep experiments agree well with the stress amplitudes for $G' = G''$ in the oscillatory stress sweep experiments (Fig. 5.1.2.7), as previously reported for other particulate gels [151].

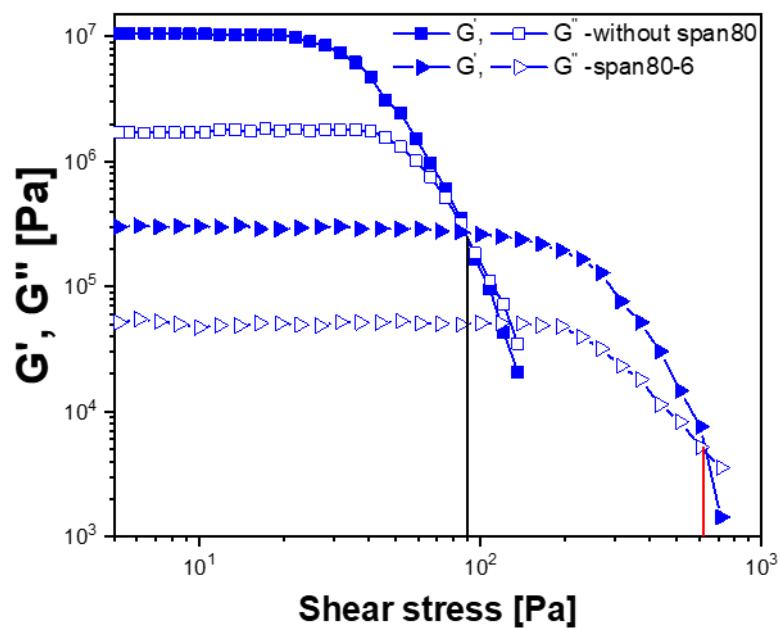


Fig.5.1.2.7 Stress amplitude sweeps for castor oil-based inks at fixed angular frequency $\omega = 1$ rad/s.

5.1.2.3 Wall slip

Slip velocity measurements were performed as described in Section 4.1.3. Video snapshots taken using the setup shown in Figure 5.1.2.8 allowed for an observation of paste motion (data summarized in Figure 5.1.2.9). By comparing the position of the red line, no movement of the upper plate is seen below 200 Pa. The sharp increase of the rotation speed sets the critical slip stress $\sigma_c \approx 200$ Pa. Above this value, the upper plate is moving. However, there is basically no deformation in the 2mm thick paste layer. Between 200 and 800 Pa, only the thin paste layer adjacent to the smooth upper plate is sheared. Similar observations have been reported earlier for microgel pastes [153, 154]. Between 800 and 1000 Pa, a second thin layer is sheared next to the lower plate with a much lower velocity than the upper interface. For $\sigma > 1000$ Pa, the sample is spilled out of the gap.

Therefore, the following discussion will be limited to the shear stress range between 400 and 800 Pa, where only the thin layer at the interface between the sample and the upper plate is sheared. The added stearin wax grease can be used as a lubricant. The slip velocity on paraffin oil-based inks with and without stearin wax in stainless steel plates in the shear stress range below σ_y is shown in the Fig.5.1.2.9, which clearly shows that the stearin wax particles promote the slip of the paste. Similar results were obtained with a PDMS-based system (data not shown).

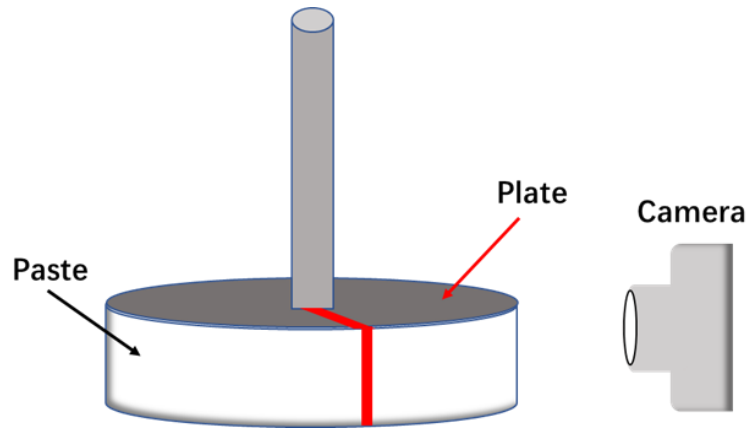


Figure 5.1.2.8 The experiment setting for observation of the wall slip phenomena and the shear profile of the sample between plates.

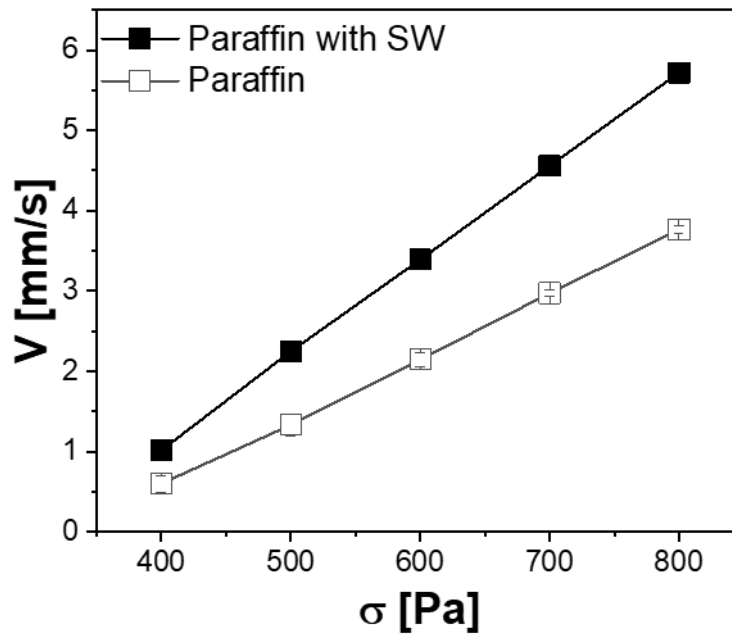


Figure 5.1.2.9 Average slip velocities for paraffin oil-based ink and without stearin wax paste calculated from measurements at 2 mm gap size. Lines are included to guide the eyes.

5.1.2.4 Viscosity

In order to realize fine 3D printing of solid electrolyte material LLZTO, three different formulations of inks were designed to satisfy the desired rheological properties of shear thinning. This feature ensures that the ink is easily extruded

into filaments by the DIW printer, and the printed structure is accurate without deformation. The flow and corresponding viscosity data of the inks are shown in Fig. 5.1.2.10. Obviously, all three differently formulated inks exhibit weak shear-thinning behavior over a wide range of medium and high shear rates, with viscosity values between 3 Pa s and 30 Pa s.

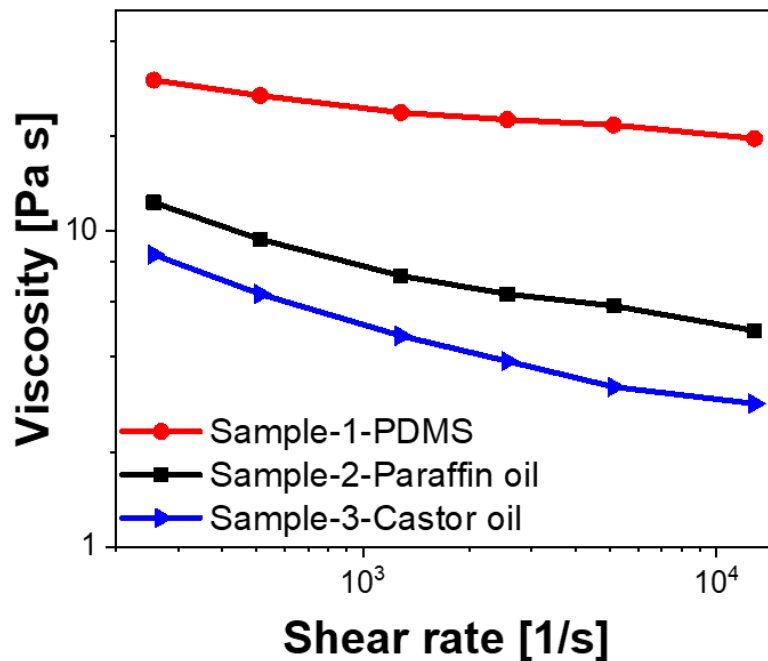


Fig.5.1.2.10 Viscosity vs. shear rate for the three investigated inks used for printing trials with PDMS, paraffin oil and castor oil as bulk fluid phase. For full description of sample composition see Table 3.3.1.

5.1.3 Structural features of DIW 3D printed samples

Geometric scaffolds for electrolyte

LLZTO is one of the excellent solid-state electrolyte materials. Typically, the electrolyte scaffolds are fabricated by manufacturing processes which restrict the dimensions in 2D. To this end, we innovatively propose a process for fabricating three-dimensional complex structures using DIW. In order to achieve this goal, we first design the required 3D printing structure through drawing

software, and then according to the characteristics of DIW printers, considering factors such as process feasibility and structural differences, we designed three polygonal geometries as shown in Fig. 5.1.3.1: honeycomb structure, triangular structure and log pile structure. The framework is constructed layer by layer by extruding ink, and the stability of the filaments and the maximum span between the filaments during the DIW printing process are tested, Note, that the filaments of the adjacent layers of the log-pile structure are perpendicular to each other.

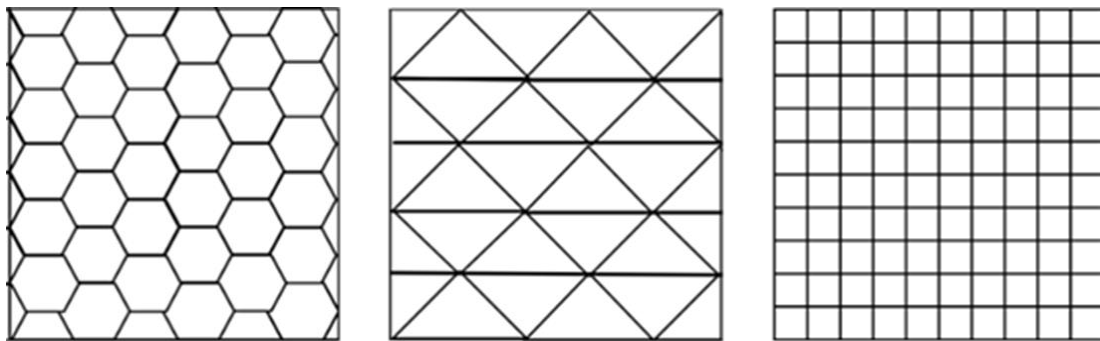


Fig. 5.1.3.1 The structure design of honeycomb, triangle, and square-shaped log pile patterns.

In order to achieve DIW 3D printing and to be able to obtain structures that exactly match the design, we designed inks with addition of secondary phases or dispersants, instead of using inks with pure suspensions. By adding a secondary phase fluid or dispersant (for composition see Table.3.3.1), we can adjust the rheological properties of the ink, so that the ink can print out the three-dimensional graphic structure using nozzles of 250 μm , 200 μm , and 150 μm in diameter.



Fig. 5.1.3.2 Macromorphology of sintered honeycomb, triangular and log-pile structures printed with the PDMS-based ink described in Table 3.3.1.

3D cuboids were successfully printed by nozzles with diameters of 400 μm , 200 μm , and 150 μm . Fig. 5.1.3.2 shows the physical picture of the samples after printing. Both capillary suspension-based inks and surfactant-added inks print frames without visible cracks that do not collapse, and the shape of the open area in each plane (xy , xz , yz) shows good accuracy. This is attributed to the unique rheological properties of the inks (high yield stress and storage modulus, shear thinning, and wall slip), and these inks are therefore considered suitable for extrusion and direct ink writing.

5.1.4 Sintering and characterization of samples

By comparing the integrity of the printed samples and the accuracy of the opening pattern, the final 150 μm nozzle was selected to print the subsequent experimental samples since it provided the highest accuracy. All printed green bodies of different structures were dried, thermally debinded and sintered (see Table 5.1.4.1 for the sintering process).

Table 5.1.4.1 Sintering process for all the samples

	Debinding	Sintering
Temperature	800 °C	900/1000/1100/1200 °C
Heating rate	1 °C / min	1 °C / min
Holding time	0.5h - 6h	0.5h - 15h

During the process of debinding and sintering, the oven temperature rises evenly to prevent the sample from being damaged by drastic temperature changes. When the temperature reaches the preset temperature, it is kept for the corresponding time. After the oven temperature has completely dropped to room temperature, the sample is removed from the oven. After measurement, it can be seen that the sample shrinks uniformly (9-17%, see Table 5.1.4.2 below).

Table 5.1.4.2. Microstructural properties of sintered samples (sintering condition: $T_s = 1100\text{ °C}$, 15 h).

Ink	Strut porosity ϵ_s (%)	Pore size $X_{50,3}$ (μm)
PDMS	47.4 ± 1.7	14.6 ± 0.2
Paraffin oil	59.8 ± 2.1	30.1 ± 0.7
Castor oil	51.9 ± 1.6	16.5 ± 0.5

Corresponding values of porosity and pore size within the printed filaments are also summarized in Table 5.1.4.2. These characteristics are related to the sintering conditions as well as the size and volume fraction of the particles in the printing ink used. The combination of direct ink writing and custom inks can precisely print complex structural frameworks with well-defined internal porosity and pore sizes. Fig 5.1.4.1 shows the macroscopic morphology of the sintered sample, (a) is the macroscopic morphology of the castor oil-based ink 3D

printed honeycomb structure frame after sintering; (b) is the side view of the triangular structure sintered body printed with PDMS-based ink; (c) is the light perspective view of the sintered body of the original log-pile structure printed with paraffin oil-based ink. The different structures printed by the three inks obtained similar sintered body samples, and no defects or deformations visible to the naked eye were found in the obtained sintered body topography images, and there was no obvious collapse and blockage of geometric openings in the three-dimensional structure. This also proves that all the inks designed have achieved the expected goals and realized the complex three-dimensional structure of DIW 3D printing with LLZTO materials.

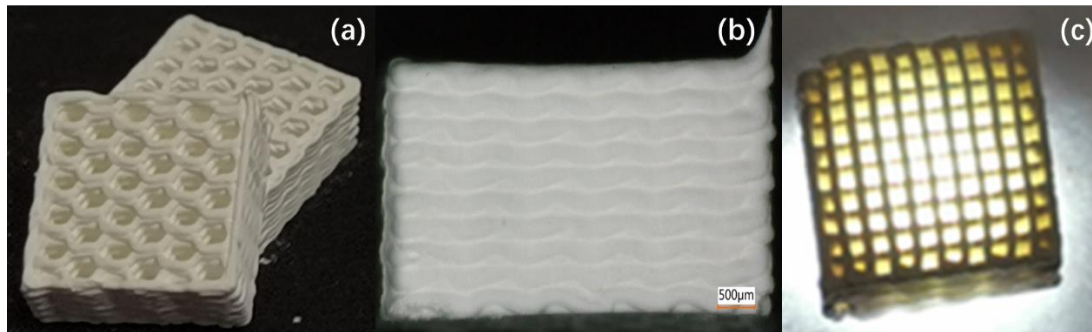


Fig.5.1.4.1 Macroscopic morphology of sintered honeycomb printed sample with different ink (from left to right ink is castor oil, PDMS, paraffin oil).

Fig. 5.1.4.2 is the cross-sectional SEM image of the 3D printed ceramic scaffold filament after sintering. The microscopic shape of different inks at the same sintering temperature and the same sintering time is slightly different, due to the different content of LLZTO powder and the difference in the bulk phase.

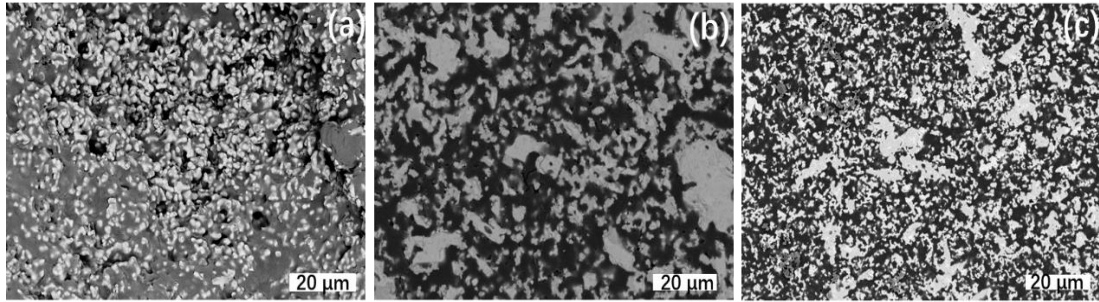


Fig.5.1.3.2 Crosscut SEM image of sintered honeycomb struts obtained from inks based on (a) PDMS; (b) paraffin oil; (c) castor oil. Sintering condition: $T_s = 1100\text{ }^\circ\text{C}$, 15 h, for ink composition refer to Table 3.3.1.

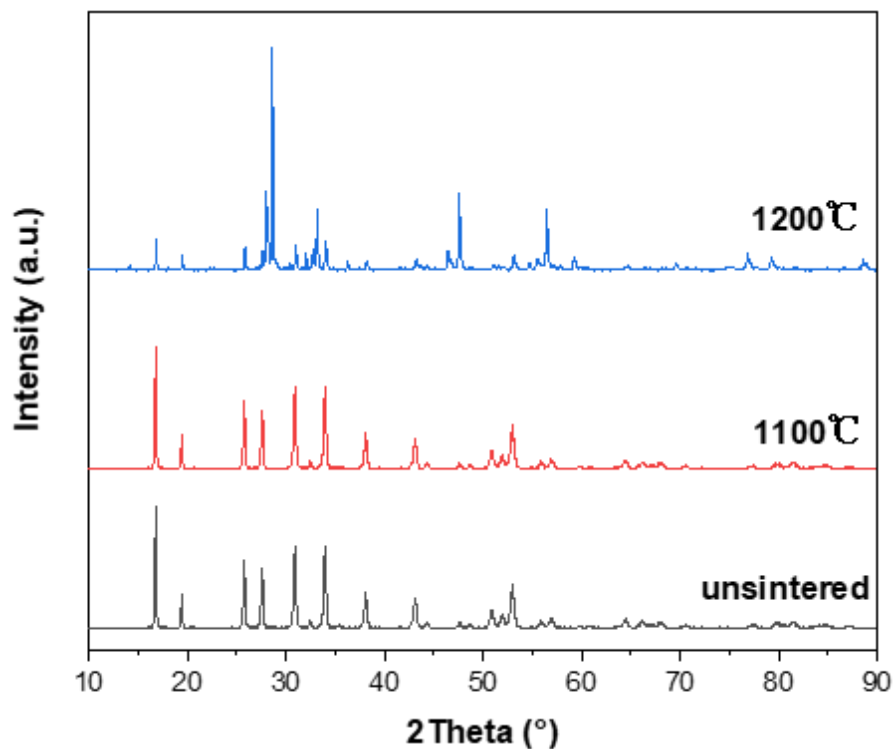


Fig.5.1.4.3 Powder XRD result of finely ground pellets unsintered (black), sintered at $1100\text{ }^\circ\text{C}$ (red) and $1200\text{ }^\circ\text{C}$ (blue) for 15 h.

Fig. 5.1.4.3 shows the XRD spectra of the raw material and samples sintered at $1100\text{ }^\circ\text{C}$ and $1200\text{ }^\circ\text{C}$ for 15 h, recording a wide range of scattering angles 2θ ($10^\circ \leq 2\theta \leq 90^\circ$). From the XRD spectrum, it can be seen that the

unsintered powder exhibits the expected scattering pattern of LLZTO[155], which is consistent with the standard cubic LLZTO diffraction peak (PDF# 80-0457), and sintering at 1100 °C does not change the crystal structure even after 15 hours. However, after sintering at 1200 °C for 15 h, a transition from a pure cubic phase to a mixed cubic and tetragonal phase occurs.

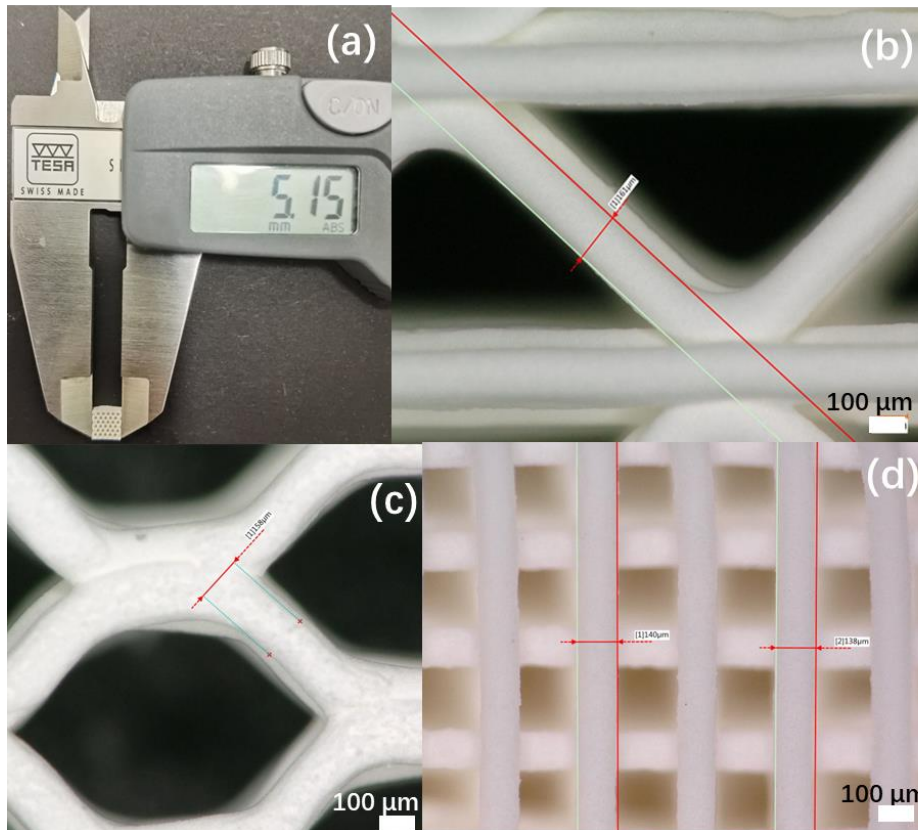


Fig. 5.1.4.4 (a) Macroscopic dimensions of the honeycomb structure sample made from the castor oil-based ink; (b), (c), (d) LSM images of filament size and morphology of samples printed from paraffin oil-based ink.

For the honeycomb scaffold made of castor oil-based ink, an example of the dimensions after sintering is shown in Fig. 5.1.4.4a, similar results were obtained for other types of ink. The dimensions of the sintered bodies were 5.15 mm × 5.15 mm × 1.8 mm with a standard deviation of ± 0.28 mm. Laser scanning microscope (LSM) images were used to assess the quality and size of printed samples. Panels b and c confirm that the printed filaments have a

smooth surface without cracks and are well connected to the underlying vertical filaments. More importantly, no visible cracks are observed at the junctions. For a nozzle diameter of 150 μm , the pillar width of the sintered body was 150 $\mu\text{m} \pm 11 \mu\text{m}$, indicating the high precision of the printing process when using this type of ink.



Fig. 5.1.4.5 V-shaped test structure for determination of the critical span distance, i.e. the span up to which no significant deformation or breakage is observed by visual inspection, exemplarily shown for filaments printed from the paraffin oil-based ink. The composition of all inks used in these printing experiments is given in Table 3.3.1.

Benefiting from the high yield stress and modulus of the ink, the filaments in each layer are very stable against deformation caused by gravity. This was further demonstrated by extruding parallel filaments on a V-shaped support layer consisting of two filaments diverging at an angle of 143° . Based on visual inspection, a filament with a width of 150 μm can be supported on a bridge with a pitch of 2200 μm without significant deformation or breakage (Fig. 5.1.4.5), i.e. a critical span $L/D \approx 15$ is achieved using this ink. Due to external factors such as the stability of the console, this value is somewhat lower than the theoretically predicted $L/D = 20$ value calculated from Equation (1) based on

the inks density and shear modulus:[13, 15]

$$G' \geq 1.4 \rho g (L/D)^4 D \quad (1)$$

where ρ is the density (Table 5.1.4.2), g is the constant of gravity, L is the length of an undeflected filament and D is the filament diameter. Critical span, modulus and density values for all three investigated inks are summarized in Table 5.1.4.3

Table 5.1.4.3 The equation parameters of the three inks.

Ink	PDMS	Paraffin oil	Castor oil
G' (Pa)	1.78×10^5	7.25×10^5	1.21×10^5
ρ (g cm⁻³)	2.2	2.1	2.8
L (μm)	1300	2200	1000
L/D (true)	9	15	7
L/D (theoretical)	14	20	12

5.1.5 Mechanical properties of DIW 3D printed samples

Compression tests were carried out for the sintered printed scaffolds in order to characterize the mechanical properties. The 3D printed honeycomb structure frame is composed of 30 hexagonal cells, the triangular structure frame is composed of 20 triangular cells, and the square log pile structure frame is composed of 100 square cells. The compressive stress-strain curve shown in Fig. 5.1.5.1 is obtained after loading the sample perpendicular to the cell direction ("in-plane"). Although all structural frames were printed with a 150 μm nozzle and had similarly sized green bodies, there were significant differences in the compressive stress-strain curves obtained for the 3D printed ceramic frames of different structures. The initial nonlinear increase in stress at strain $\epsilon < 0.2$ may be due to the orientation of the experimental setup at low loads. The printed structures exhibit elastic deformation at strain $\epsilon > 0.2$. As the stress increases, the lattice begins to crack and eventually fails. Table 5.1.5.1 summarizes the compressive strength data for three different structures printed with different inks and sintered at different temperatures.

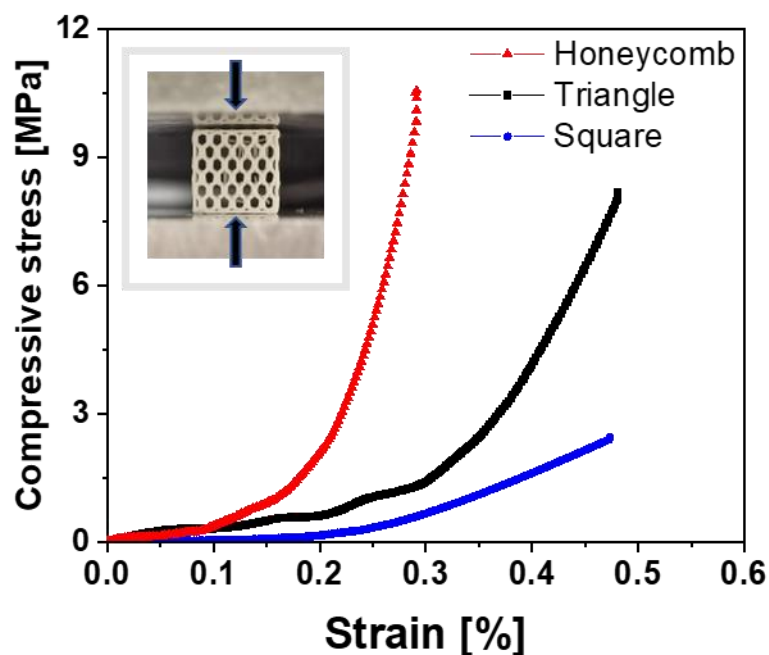


Fig. 5.1.5.1 Compressive stress-strain curves of PDMS-based 3D printed structures (sintering condition: $T_s = 1100\text{ }^\circ\text{C}$, 15 h)

Table 5.1.5.1 The compressive strength of the sample after sintering for 15h.

Compressive strength (MPa)	T (°C)	Honeycomb	Triangle	Log pile
	PDMS	900	4.1 ± 0.2	2.1 ± 0.5
1000		6.7 ± 0.6	5.5 ± 0.7	1.6 ± 0.4
1100		10.7 ± 1.4	8.2 ± 0.9	2.4 ± 0.1
Paraffin oil	900	0.7 ± 0.2	0.5 ± 0.5	0.2 ± 0.1
	1000	1.5 ± 0.2	1.1 ± 0.5	0.6 ± 0.4
	1100	2.9 ± 0.1	1.9 ± 0.1	0.7 ± 0.1
Castor oil	900	1.0 ± 0.1	0.5 ± 0.4	0.2 ± 0.1
	1000	1.7 ± 0.2	1.3 ± 0.4	0.6 ± 0.3
	1100	5.1 ± 0.1	2.7 ± 0.4	1.2 ± 0.2

From the data in Table 5.1.5.1 and the histogram analysis in Fig.5.1.5.2, it can be seen that the fracture stress of the honeycomb structure is significantly higher than that of the triangle and square structures, and this phenomenon is observed for all three investigated inks. This is well known in literature [156]. This phenomenon is attributed to the more uniform stress distribution and tighter connections in the honeycomb structure compared to the triangular structure, which facilitates the stress dispersion. And the log pile samples are even weaker due to the 90° rotation of the adjacent layers. The log pile structure is more prone to stress concentration than the triangular structure due to the 90° rotation of adjacent layers, so its fracture stress is lower than that of the other two structures.

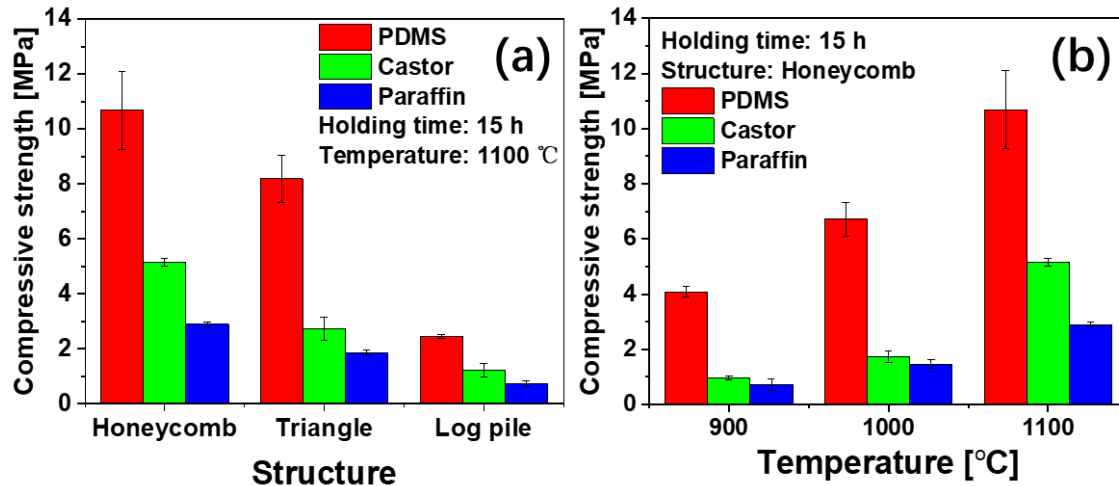


Fig.5.1.5.2 Compressive properties and compressive strength of 3D printed lattices with different structures: (a) Compressive strength of different cellular structures 3D printed with three different inks (sintering condition: $T_s = 1100$ °C, 15 h; (b) Compressive strength of 3D printed structures made from different inks after sintering at three different temperatures. For ink composition see Table 3.3.1.

The compressive strength of the honeycomb structure 3D printed using different types of inks were compared after sintering at different temperatures. It can be clearly seen from the histogram in Fig.5.1.5.2b that at the same sintering temperature, the honeycomb structure made of PDMS ink is obviously stronger than the honeycomb structure based on paraffin and castor ink. Combining with Table 5.1.5.2, it can be seen that the similar trend was obtained for the other cell structures, PDMS ink always produces the samples with the highest compressive strength. Within the range of experimental uncertainty, comparing the data of the same honeycomb structure and sintering temperature, the compressive strength values of the hydrocarbon oil-based ink samples are basically the same. In addition, the compressive strength of the PDMS-based 3D printed lattice increases significantly with increasing sintering temperature. The same trend was observed for samples made with other inks, but with lower absolute compressive strength values.

Table 5.1.5.2 The total porosity ϵ^* and shrinkage of the Honeycomb structure sample after sintering for 15 hours.

Sintering Temp. (°C)	PDMS		Paraffin oil		Castor oil	
	True ϵ^* (%)	Shrinkage (%)	True ϵ^* (%)	Shrinkage (%)	True ϵ^* (%)	Shrinkage (%)
900	78.4 ± 0.4	11.4 ± 0.54	83.2 ± 0.7	9.0 ± 0.3	82.9 ± 0.49	10.9 ± 0.4
1000	75.3 ± 0.2	15.0 ± 0.8	80.5 ± 0.3	11.4 ± 0.5	79.3 ± 0.4	13.8 ± 0.4
1100	72.9 ± 0.2	17.0 ± 1.0	76.4 ± 0.2	13.8 ± 0.8	75.1 ± 0.2	16.2 ± 0.8

According to the data summarized in Table 5.1.5.2, as the sintering temperature increases, the porosity decreases and the shrinkage increases for all samples. As a result, a denser structure can be obtained at higher sintering temperatures, and denser samples usually also have higher strength. The shrinkage and porosity of the sintered bodies obtained by the same sintering process with different inks vary considerably. With a given lattice structure and a fixed sintering temperature, the strength of sintered bodies made with different inks increases with decreasing porosity. Notably, despite the low solid content in PDMS-based inks (see Table 3.3.1), the honeycomb structures made from PDMS-based inks exhibited the lowest porosity and highest strength. This is because the PDMS-based ink contains a large amount of silicone oil ($[\text{C}_2\text{H}_6\text{OSi}]_n$) in the bulk phase, which is different from the bulk phase of the other two inks, which are hydrocarbons. The silicone oil does not burn during sintering, therefore, a lot of silicon remained in the samples after sintering finally resulting in lower porosity and hence higher strength of the printed cellular structures.

Table 5.1.5.3. EDX results of the samples (all results in atomic %; Sample 1: LLZTO, Sample 2: LLZTO+ bulk phase, Sample 3: LLZTO+ bulk phase+ second phase).

	Sample 1	Sample 2	Sample 3
Si	0	12.75	12.46
La	19.02	17.80	17.82
Zr	4.26	3.80	3.85
Ta	0.85	0.69	0.78
O	75.87	64.96	65.09

This was also confirmed by EDX spectral analysis, as shown in Table 5.1.5.3. The addition of secondary fluid does not significantly affect the silicon content in the sintered samples. This contribution of extra Si in the solid phase in the sintered samples may also be the reason for the smaller pore size of samples made with PDMS-based inks compared to hydrocarbon oil-based inks (see Table 5.1.3.2).

5.2 SLA 3D printing LLZTO

In cooperation with Lithoz company it was aimed to jointly develop a photocurable resin suitable for SLA 3D printing of LLZTO. Due to confidentiality terms the complete resin formula was not disclosed. Paraffin oil-based, PDMS-based and castor oil-based suspensions containing LLZTO powder were submitted to the company for processing into photocurable resins. Wherein the solid content of the suspension is 40 vol%. Through multiple experiments, a sample matching the design structure was successfully printed by SLA, as shown in Fig. 5.2.1. However, due to factors such as high resin viscosity and unstable performance, the printing repetition rate is low, and the designed structure cannot be manufactured reproducibly, so the final development failed.

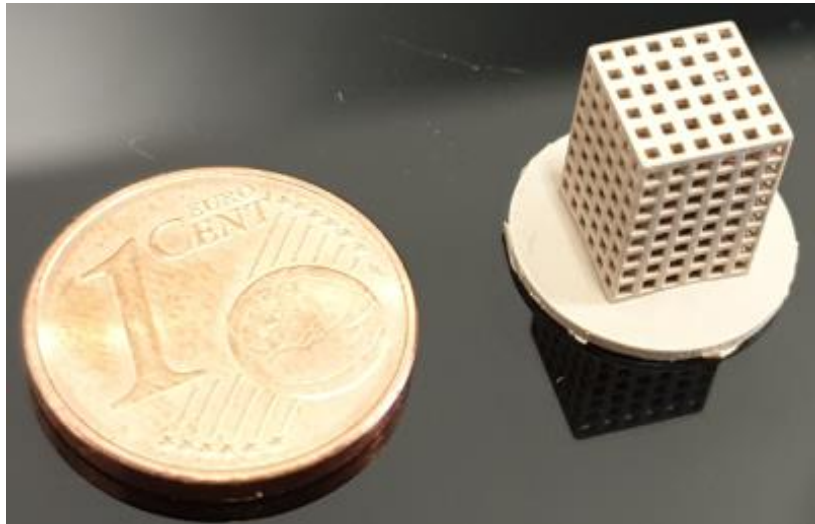


Fig. 5.2.1 SLA 3D printing LLZTO spatial three-dimensional structure physical picture.

5.3 FDM 3D printing LLZTO

Table 5.3.1 shows all the feasible formulas tried by FDM 3D printing LLZTO materials. From Table 5.3.1, it can be clearly found that the goal of FDM 3D printing LLZTO materials has not been achieved.

Table 5.3.1 FDM 3D printing experimental formula

Particles	Bulk phase	Second phase	3D-printing
LLZTO (26%-40%)	TPU	DMF	x
LLZTO (26%-40%)	TPU	DMSO	x
LLZTO (26%-40%)	TPU	Acetone	x
LLZTO (26%-40%)	ABS	Butadiene	x
LLZTO (26%-40%)	PLA	chloroform	x

Due to the high processing temperature of LLZTO, after the heating process, it fails to melt to form a filamentous material that can be printed through the nozzle in a molten state. The similar problem also occurred in the process of dissolving

thermoplastic polyurethanes (TPU) and polylactic acid (PLA) to make filaments, neither of which succeeded in obtaining thermoplastic filaments that could pass through the nozzle. When co-blending acrylonitrile butadiene styrene (ABS) with LLZTO material was attempted in a screw extruder, LLZTO was difficult to be uniformly dispersed in ABS, and the processed thermoplastic filament could not be printed continuously by FDM, and the filament tended to clog the nozzle during the melting process, so FDM 3D printing with LLZTO material has not been successfully achieved.

Chapter 6:

Conclusions

In summary, in the first part, we describe in detail the fabrication of complex three-dimensional ordered structures using DIW 3D printed solid electrolytes which can potentially be used to replace the conventional casting, molding, or extrusion methods which can only be used for fabricating planar geometries. Three ink formulations suitable for high-precision DIW-type additive manufacturing based on LLZTO powders were developed. Capillary suspension, that is, a ternary solid/fluid/fluid system, forms a particle network controlled by capillary forces which determines the rheological properties of the ink. Two kinds of inks are made based on this special concept, PDMS and paraffin oil are used as the main fluid phase. Ethylene glycol and DMF were used as the secondary liquid phases, respectively. In both cases, stearic wax particles were added as a lubricant and soft filler suspended in the bulk phase. The third type of ink is a binary suspension of LLZTO powder in castor oil, to which a non-ionic dispersant is added to control particle dispersion, thereby changing the rheology of the ink.

All three ink formulations exhibit significant shear thinning as well as high yield stresses ($\sigma_y > 1000$ Pa) and shear moduli ($G' > 10^5$ Pa). According to the different requirements of printing and structure, these properties can be easily adjusted in a wide range by adjusting the ratio of secondary fluid/dispersant and hard wax resin. A three-dimensional grid structure was successfully printed using DIW technology with a nozzle diameter of 150 μm , and the printed filaments benefited from the high yield stress and high storage modulus of the ink resulting in a high shape accuracy. Therefore, the printed structural frame does not deform and collapse, and finally a printed green body with high stability

is obtained. Filaments span L/D between 7 and 15 depending on the ink selected. After mastering the green sintering process, no deformation or crack formation occurred in the samples after debinding and sintering. As expected, when compared at the same sintering temperature and ink composition, the honeycomb structure exhibited higher strength than the triangular structure, which in turn was stronger than the log-pile structure. Also, under the same structure and ink composition, the compressive strength of the samples increases with increasing sintering temperature. The compressive strength of the samples increases with decreasing porosity, and hence the cellular structures made from PDMS-based inks are always stronger than those made from other inks due to the residual silicon in the samples after sintering, resulting in lower porosity.

Through the design of the ink composition, the DIW printing properties of rheology and extrusion can be fine-tuned, and various complex structures ranging from simple square grids to hexagonal honeycombs can be explored and built. It should be noted that these LLZTO-based ink formulations are not special, and they can also be used to print other ceramic materials. Here, we demonstrate that these inks offer the possibility to simplify the fabrication of solid electrolytes, improve mechanical properties, construct diverse high-precision structures, and also provide a basis for the design and preparation of ceramic-polymer hybrid electrolytes.

Chapter 7:

Outlook

The successful realization of processing $\text{Li}_{6.4}\text{La}_3\text{Zr}_{1.4}\text{Ta}_{0.6}\text{O}_{12}$ (LLZTO) via 3D printing and the formulation of the corresponding inks is the highlight of this thesis. The LLZTO material can be printed using the direct ink writing (DIW) technique, which provides a structural basis for ceramic-polymer hybrid electrolytes and a new idea for the development of ceramic solid-state electrolytes, but there are still some regrets in this thesis due to limitations such as time and experimental equipment.

The failure of FDM and SLA printing proves that the road to 3D printing LLZTO materials is still full of challenges and opportunities. For the fabrication of FDM printable thermoplastic filaments, the utilization of a twin-screw extruder with better exhaust performance and better extrusion stability can be considered in the future trying to overcome the problem of non-uniform particle dispersion during LLZTO processing. Avoiding the entrainment of air bubbles during the blending process is another challenge in future developments. A new print head design for the FDM printer may be attempted in order to avoid demixing of particles and polymer upon melting and nozzle clogging.

Although occasionally successful in printing the designed structure using SLA, there are still difficulties to overcome in order to establish a successful 3D printing route. The interaction between the LLZTO particles and the reactive resin are still not understood. The chemical reactions among these species need to be investigated in order to develop a resin tailor-made for the LLZTO particles. In the future, we will learn more about light-curing resins and try to break the blockade to be able to develop our own light-curing resins for SLA 3D printing. By improving the rheological properties of the resin to obtain the final

printable LLZTO light-curing resin, and achieve successful printing of the designed structures.

Since ceramic materials are brittle, they may be combined with polymer materials to improve the mechanical properties, particularly the toughness of the composite. Therefore, hybrid ceramic polymer electrolytes have a broad application prospect. The success of 3D printed ceramic electrolyte materials offers unlimited possibilities for mixed ceramic polymer solid state electrolytes. Future high ionic conductivity between electrodes is ensured by ceramic channels that provide continuous, uninterrupted pathways for Li ion transport. The polymer material may also serve to prevent electrode dendrite growth from piercing the electrolyte. To provide a practical approach for new all-solid-state lithium-ion batteries.

The lack of a complete electrochemical laboratory and related knowledge has prevented the completion of electrochemistry-related testing of the printed structures, which is a major regret of this thesis. In the future, by learning electrochemistry-related knowledge, we will be able to understand all aspects of the printed ceramic structure, and then improve the ink formulation and improve the designed structure in a more targeted manner. To truly realize 3D printing of ceramic solid electrolytes with designable structure, adjustable precision and excellent performance.

References

1. Blomgren, G.E., *The development and future of lithium ion batteries*. Journal of The Electrochemical Society, 2016. **164**(1): p. A5019.
2. Goodenough, J.B. and K.-S. Park, *The Li-Ion Rechargeable Battery: A Perspective*. Journal of the American Chemical Society, 2013. **135**(4): p. 1167-1176.
3. Li, M., et al., *30 Years of Lithium-Ion Batteries*. Advanced Materials, 2018. **30**(33): p. 1800561.
4. Zheng, F., et al., *Review on solid electrolytes for all-solid-state lithium-ion batteries*. Journal of Power Sources, 2018. **389**: p. 198-213.
5. Armand, M. and J.M. Tarascon, *Building better batteries*. Nature, 2008. **451**(7179): p. 652-657.
6. Wang, Q., et al., *Thermal runaway caused fire and explosion of lithium ion battery*. Journal of Power Sources, 2012. **208**: p. 210-224.
7. Motavalli, J., *Technology: A solid future*. Nature, 2015. **526**(7575): p. S96-S97.
8. Manthiram, A., X. Yu, and S. Wang, *Lithium battery chemistries enabled by solid-state electrolytes*. Nature Reviews Materials, 2017. **2**(4): p. 16103.
9. Kasper, H., *Series of rare earth garnets $Ln_3+ 3M_2Li+ 3O_{12}$ ($M= Te, W$)*. Inorganic Chemistry, 1969. **8**(4): p. 1000-1002.
10. Deviannapoorani, C., et al., *Lithium ion transport properties of high conductive tellurium substituted $Li_7La_3Zr_2O_{12}$ cubic lithium garnets*.

- Journal of Power Sources, 2013. **240**: p. 18-25.
11. Schnell, J., et al., *Prospects of production technologies and manufacturing costs of oxide-based all-solid-state lithium batteries*. 2019. **12**(6): p. 1818-1833.
 12. Depla, D. and S. Mahieu, *Reactive sputter deposition*. Vol. 109. 2008: Springer.
 13. Chen, B. and N. Willenbacher, *High-precision direct ink writing of $\text{Li}_6.4\text{La}_3\text{Zr}_{1.4}\text{Ta}_{0.6}\text{O}_{12}$* . Journal of the European Ceramic Society, 2022. **42**(16): p. 7491-7500.
 14. Minas, C., et al., *3D Printing of Emulsions and Foams into Hierarchical Porous Ceramics*. Advanced Materials, 2016. **28**(45): p. 9993-9999.
 15. Smay, J.E., J. Cesarano, and J.A. Lewis, *Colloidal Inks for Directed Assembly of 3-D Periodic Structures*. Langmuir, 2002. **18**(14): p. 5429-5437.
 16. Dahn, J., R. Fong, and M. Spoon, *Suppression of staging in lithium-intercalated carbon by disorder in the host*. Physical Review B, 1990. **42**(10): p. 6424.
 17. Ohzuku, T., Y. Iwakoshi, and K. Sawai, *Formation of lithium-graphite intercalation compounds in nonaqueous electrolytes and their application as a negative electrode for a lithium ion (shuttlecock) cell*. Journal of The Electrochemical Society, 1993. **140**(9): p. 2490.
 18. Nzereogu, P.U., et al., *Anode materials for lithium-ion batteries: A review*. Applied Surface Science Advances, 2022. **9**: p. 100233.

19. Fergus, J.W., *Recent developments in cathode materials for lithium ion batteries*. Journal of power sources, 2010. **195**(4): p. 939-954.
20. Marcinek, M., et al., *Electrolytes for Li-ion transport – Review*. Solid State Ionics, 2015. **276**: p. 107-126.
21. Zhang, S.S., *A review on the separators of liquid electrolyte Li-ion batteries*. Journal of power sources, 2007. **164**(1): p. 351-364.
22. Liu, C., Z.G. Neale, and G. Cao, *Understanding electrochemical potentials of cathode materials in rechargeable batteries*. Materials Today, 2016. **19**(2): p. 109-123.
23. Dunn, B., H. Kamath, and J.-M. Tarascon, *Electrical energy storage for the grid: a battery of choices*. Science, 2011. **334**(6058): p. 928-935.
24. Horiba, T., *Lithium-Ion Battery Systems*. Proceedings of the IEEE, 2014. **102**(6): p. 939-950.
25. Whittingham, M.S., *Electrical energy storage and intercalation chemistry*. Science, 1976. **192**(4244): p. 1126-1127.
26. Thackeray, M.M., et al., *Lithium insertion into manganese spinels*. Materials Research Bulletin, 1983. **18**(4): p. 461-472.
27. Yoshino, A., *The Lithium-ion Battery: Two Breakthroughs in Development and Two Reasons for the Nobel Prize*. Bulletin of the Chemical Society of Japan, 2022. **95**(1): p. 195-197.
28. Xu, K., *Nonaqueous Liquid Electrolytes for Lithium-Based Rechargeable Batteries*. Chemical Reviews, 2004. **104**(10): p. 4303-4418.

29. Ahniyaz, A., et al., *Progress in solid-state high voltage lithium-ion battery electrolytes*. Advances in Applied Energy, 2021. **4**: p. 100070.
30. Lin, Y., et al., *Organic liquid electrolytes in Li-S batteries: actualities and perspectives*. Energy Storage Materials, 2021. **34**: p. 128-147.
31. Chen, Y., et al., *A review of lithium-ion battery safety concerns: The issues, strategies, and testing standards*. Journal of Energy Chemistry, 2021. **59**: p. 83-99.
32. Kuboki, T., et al., *Lithium-air batteries using hydrophobic room temperature ionic liquid electrolyte*. Journal of Power Sources, 2005. **146**(1): p. 766-769.
33. Smitha, B., S. Sridhar, and A. Khan, *Solid polymer electrolyte membranes for fuel cell applications—a review*. Journal of membrane science, 2005. **259**(1-2): p. 10-26.
34. Manuel Stephan, A., *Review on gel polymer electrolytes for lithium batteries*. European Polymer Journal, 2006. **42**(1): p. 21-42.
35. Tarascon, J.-M. and M. Armand, *Issues and challenges facing rechargeable lithium batteries*. nature, 2001. **414**(6861): p. 359-367.
36. Xia, S., et al., *Practical Challenges and Future Perspectives of All-Solid-State Lithium-Metal Batteries*. Chem, 2019. **5**(4): p. 753-785.
37. Ratner, M.A., P. Johansson, and D.F. Shriver, *Polymer electrolytes: ionic transport mechanisms and relaxation coupling*. Mrs Bulletin, 2000. **25**(3): p. 31-37.

38. Meyer, W.H., *Polymer electrolytes for lithium-ion batteries*. Advanced materials, 1998. **10**(6): p. 439-448.
39. MacGlashan, G.S., Y.G. Andreev, and P.G. Bruce, *Structure of the polymer electrolyte poly(ethylene oxide)₆:LiAsF₆*. Nature, 1999. **398**(6730): p. 792-794.
40. Mehrer, H., *Diffusion in solids: fundamentals, methods, materials, diffusion-controlled processes*. Vol. 155. 2007: Springer Science & Business Media.
41. Wu, M., B. Xu, and C. Ouyang, *Physics of electron and lithium-ion transport in electrode materials for Li-ion batteries*. Chinese Physics B, 2015. **25**(1): p. 018206.
42. Park, M., et al., *A review of conduction phenomena in Li-ion batteries*. Journal of power sources, 2010. **195**(24): p. 7904-7929.
43. Manthiram, A., X. Yu, and S. Wang, *Lithium battery chemistries enabled by solid-state electrolytes*. Nature Reviews Materials, 2017. **2**(4): p. 1-16.
44. Quartarone, E. and P. Mustarelli, *Electrolytes for solid-state lithium rechargeable batteries: recent advances and perspectives*. Chemical Society Reviews, 2011. **40**(5): p. 2525-2540.
45. Hu, Y.-S., *Batteries: getting solid*. Nature Energy, 2016. **1**(4): p. 1-2.
46. Fergus, J.W., *Ceramic and polymeric solid electrolytes for lithium-ion batteries*. Journal of Power Sources, 2010. **195**(15): p. 4554-4569.
47. Xia, W., et al., *Ionic conductivity and air stability of Al-doped Li₇La₃Zr₂O₁₂*

- sintered in alumina and Pt crucibles*. ACS applied materials & interfaces, 2016. **8**(8): p. 5335-5342.
48. Matsuyama, T., et al., *Electrochemical properties of all-solid-state lithium batteries with amorphous titanium sulfide electrodes prepared by mechanical milling*. Journal of Solid State Electrochemistry, 2013. **17**(10): p. 2697-2701.
49. Kanehori, K., et al., *Titanium disulfide films fabricated by plasma CVD*. Solid State Ionics, 1986. **18**: p. 818-822.
50. Ohtsuka, H. and J.-i. Yamaki, *Electrical characteristics of Li₂O V₂O₅ SiO₂ thin films*. Solid State Ionics, 1989. **35**(3-4): p. 201-206.
51. Akridge, J.R. and H. Vourlis, *Solid state batteries using vitreous solid electrolytes*. Solid State Ionics, 1986. **18**: p. 1082-1087.
52. Bates, J.B., et al., *Fabrication and characterization of amorphous lithium electrolyte thin films and rechargeable thin-film batteries*. Journal of Power Sources, 1993. **43**(1): p. 103-110.
53. Bates, J.B., et al., *Thin-film lithium and lithium-ion batteries*. Solid State Ionics, 2000. **135**(1): p. 33-45.
54. Magistris, A., G. Chiodelli, and M. Villa, *Lithium borophosphate vitreous electrolytes*. Journal of Power Sources, 1985. **14**(1): p. 87-91.
55. Bates, J., et al., *Preferred orientation of polycrystalline LiCoO₂ films*. Journal of The Electrochemical Society, 2000. **147**(1): p. 59.
56. Fleutot, B., et al., *Lithium borophosphate thin film electrolyte as an*

- alternative to LiPON for solder-reflow processed lithium-ion microbatteries*. Solid State Ionics, 2013. **249**: p. 49-55.
57. Yoon, Y., et al., *Characterization of lithium borophosphate glass thin film electrolytes deposited by RF-magnetron sputtering for micro-batteries*. Solid State Ionics, 2012. **225**: p. 636-640.
58. Zhang, Z. and S. Zhang, *Rechargeable batteries*. Nat Commun, 2015. **4**.
59. Alamgir, M. and K. Abraham, *Li ion conductive electrolytes based on poly (vinyl chloride)*. Journal of the Electrochemical Society, 1993. **140**(6): p. L96.
60. Capiglia, C., et al., *Structure and transport properties of polymer gel electrolytes based on PVdF-HFP and LiN (C₂F₅SO₂)₂*. Solid State Ionics, 2000. **131**(3-4): p. 291-299.
61. Feuillade, G. and P. Perche, *Ion-conductive macromolecular gels and membranes for solid lithium cells*. Journal of Applied Electrochemistry, 1975. **5**(1): p. 63-69.
62. Zhou, Y., et al., *Preparation of rechargeable lithium batteries with poly (methyl methacrylate) based gel polymer electrolyte by in situ γ -ray irradiation-induced polymerization*. Journal of applied electrochemistry, 2004. **34**(11): p. 1119-1125.
63. Chen-Yang, Y., et al., *Polyacrylonitrile electrolytes: 1. A novel high-conductivity composite polymer electrolyte based on PAN, LiClO₄ and α -Al₂O₃*. Solid State Ionics, 2002. **150**(3-4): p. 327-335.
64. Di Noto, V. and V. Zago, *Inorganic-Organic Polymer Electrolytes Based on*

- PEG400 and Al [OCH (CH₃)₂]₃: I. Synthesis and Vibrational Characterizations.* Journal of The Electrochemical Society, 2004. **151**(2): p. A216.
65. Liu, Y., J. Lee, and L. Hong, *In situ preparation of poly (ethylene oxide)–SiO₂ composite polymer electrolytes.* Journal of Power Sources, 2004. **129**(2): p. 303-311.
66. Magistris, A., et al., *Transport and thermal properties of (PEO) *n*–LiPF₆ electrolytes for super-ambient applications.* Solid state ionics, 2000. **136**: p. 1241-1247.
67. Marcinek, M., et al., *Ionic association in liquid (polyether–Al₂O₃–LiClO₄) composite electrolytes.* Solid State Ionics, 2005. **176**(3-4): p. 367-376.
68. Kumar, B. and J. Fellner, *Polymer–ceramic composite protonic conductors.* Journal of power sources, 2003. **123**(2): p. 132-136.
69. Miyake, N., J. Wainright, and R. Savinell, *Evaluation of a sol-gel derived nafion/silica hybrid membrane for proton electrolyte membrane fuel cell applications: I. Proton conductivity and water content.* Journal of the Electrochemical Society, 2001. **148**(8): p. A898.
70. Capuano, F., F. Croce, and B. Scrosati, *Composite polymer electrolytes.* Journal of the Electrochemical Society, 1991. **138**(7): p. 1918.
71. Panero, S., B. Scrosati, and S. Greenbaum, *Ionic conductivity and ⁷Li NMR Study of Poly (ethylene glycol) complexed with lithium salts.* Electrochimica Acta, 1992. **37**(9): p. 1533-1539.

72. Borghini, M.C., et al., *Electrochemical Properties of Polyethylene Oxide-Li [(CF₃SO₂)₂N]-Gamma-LiAlO₂ Composite Polymer Electrolytes*. Journal of the Electrochemical Society, 1995. **142**(7): p. 2118.
73. Golodnitsky, D., et al., *Conduction Mechanisms in Concentrated Lil - Polyethylene Oxide - Al₂O₃-Based Solid Electrolytes*. Journal of The Electrochemical Society, 1997. **144**(10): p. 3484.
74. Krawiec, W., et al., *Polymer nanocomposites: a new strategy for synthesizing solid electrolytes for rechargeable lithium batteries*. Journal of Power Sources, 1995. **54**(2): p. 310-315.
75. Wang, C., X.-W. Zhang, and A.J. Appleby, *Solvent-free composite PEO-ceramic fiber/mat electrolytes for lithium secondary cells*. Journal of The Electrochemical Society, 2004. **152**(1): p. A205.
76. Li, Q., et al., *Cycling performances and interfacial properties of a Li/PEO-Li (CF₃SO₂)₂N-ceramic filler/LiNi_{0.8}Co_{0.2}O₂ cell*. Journal of power sources, 2001. **97**: p. 795-797.
77. Kennedy, J.H., et al., *Preparation and conductivity measurements of SiS₂ Li₂S glasses doped with LiBr and LiCl*. Solid State Ionics, 1986. **18**: p. 368-371.
78. Kennedy, J.H. and Y. Yang, *A highly conductive Li⁺-glass system:(1-x)(0.4 SiS₂-0.6 Li₂S)-xLil*. J. Electrochem. Soc, 1986. **133**(11): p. 2437-2438.
79. Murayama, M., et al., *Material design of new lithium ionic conductor, thio-LISICON, in the Li₂S-P₂S₅ system*. Solid State Ionics, 2004. **170**(3-4): p.

- 173-180.
80. Ohtomo, T., et al., *Electrical and electrochemical properties of Li₂S–P₂S₅–P₂O₅ glass–ceramic electrolytes*. Journal of Power Sources, 2005. **146**(1-2): p. 715-718.
 81. Kobayashi, T., et al., *All solid-state battery with sulfur electrode and thio-LISICON electrolyte*. Journal of Power Sources, 2008. **182**(2): p. 621-625.
 82. Inada, T., et al., *All solid-state sheet battery using lithium inorganic solid electrolyte, thio-LISICON*. Journal of Power Sources, 2009. **194**(2): p. 1085-1088.
 83. Nagao, M., et al., *Characterization of all-solid-state lithium secondary batteries using CuxMo6S8–y electrode and Li₂S–P₂S₅ solid electrolyte*. Journal of Power Sources, 2009. **189**(1): p. 672-675.
 84. Kamaya, N., et al., *A lithium superionic conductor*. Nature materials, 2011. **10**(9): p. 682-686.
 85. Mizuno, F., et al., *All-solid-state lithium secondary batteries using Li₂S–SiS₂–Li₄SiO₄ glasses and Li₂S–P₂S₅ glass ceramics as solid electrolytes*. Solid state ionics, 2004. **175**(1-4): p. 699-702.
 86. Goodenough, J.B., H.-P. Hong, and J. Kafalas, *Fast Na⁺-ion transport in skeleton structures*. Materials Research Bulletin, 1976. **11**(2): p. 203-220.
 87. Thangadurai, V. and W. Weppner, *Recent progress in solid oxide and lithium ion conducting electrolytes research*. Ionics, 2006. **12**(1): p. 81-92.
 88. Abrahams, I. and E. Hadzifejzovic, *Lithium ion conductivity and thermal*

- behaviour of glasses and crystallised glasses in the system Li₂O–Al₂O₃–TiO₂–P₂O₅*. Solid State Ionics, 2000. **134**(3-4): p. 249-257.
89. Hartmann, P., et al., *Degradation of NASICON-type materials in contact with lithium metal: formation of mixed conducting interphases (MCI) on solid electrolytes*. The Journal of Physical Chemistry C, 2013. **117**(41): p. 21064-21074.
90. Aono, H., et al., *Ionic conductivity of solid electrolytes based on lithium titanium phosphate*. Journal of the electrochemical society, 1990. **137**(4): p. 1023.
91. Kobayashi, E., et al., *Electrochemical properties of Li symmetric solid-state cell with NASICON-type solid electrolyte and electrodes*. Electrochemistry communications, 2010. **12**(7): p. 894-896.
92. Arbi, K., et al., *High lithium ion conducting solid electrolytes based on NASICON Li_{1+x}Al_xM_{2-x}(PO₄)₃ materials (M= Ti, Ge and 0 ≤ x ≤ 0.5)*. Journal of the European Ceramic Society, 2015. **35**(5): p. 1477-1484.
93. Ren, Y., et al., *Oxide electrolytes for lithium batteries*. Journal of the American Ceramic Society, 2015. **98**(12): p. 3603-3623.
94. Belous, A., et al., *Investigation into complex oxides of La_{2/3-x}Li_{3x}TiO₃ composition*. Izv. Akad. Nauk SSSR, Neorg. Mater, 1987. **23**(3): p. 470-472.
95. Inaguma, Y., et al., *High ionic conductivity in lithium lanthanum titanate*. Solid State Communications, 1993. **86**(10): p. 689-693.
96. Yao, X., et al., *All-solid-state lithium batteries with inorganic solid*

- electrolytes: Review of fundamental science*. Chinese Physics B, 2015. **25**(1): p. 018802.
97. Thangadurai, V. and W. Weppner, *Li₆Ala₂Ta₂O₁₂ (A= Sr, Ba): novel garnet-like oxides for fast lithium ion conduction*. Advanced Functional Materials, 2005. **15**(1): p. 107-112.
98. Thangadurai, V., H. Kaack, and W.J. Weppner, *Novel fast lithium ion conduction in garnet-type Li₅La₃M₂O₁₂ (M= Nb, Ta)*. Journal of the American Ceramic Society, 2003. **86**(3): p. 437-440.
99. Thangadurai, V. and W. Weppner, *Effect of sintering on the ionic conductivity of garnet-related structure Li₅La₃Nb₂O₁₂ and In- and K-doped Li₅La₃Nb₂O₁₂*. Journal of Solid State Chemistry, 2006. **179**(4): p. 974-984.
100. Kaeriyama, A., et al., *Evaluation of electrochemical characteristics of Li₇La₃Zr₂O₁₂ solid electrolyte*. ECS Transactions, 2009. **16**(24): p. 175.
101. Shimonishi, Y., et al., *Synthesis of garnet-type Li_{7-x}La₃Zr₂O₁₂-1/2x and its stability in aqueous solutions*. Solid State Ionics, 2011. **183**(1): p. 48-53.
102. Kumazaki, S., et al., *High lithium ion conductive Li₇La₃Zr₂O₁₂ by inclusion of both Al and Si*. Electrochemistry communications, 2011. **13**(5): p. 509-512.
103. Murugan, R., S. Ramakumar, and N. Janani, *High conductive yttrium doped Li₇La₃Zr₂O₁₂ cubic lithium garnet*. Electrochemistry Communications, 2011. **13**(12): p. 1373-1375.

104. El Shinawi, H. and J. Janek, *Stabilization of cubic lithium-stuffed garnets of the type "Li₇La₃Zr₂O₁₂" by addition of gallium*. Journal of power sources, 2013. **225**: p. 13-19.
105. Afyon, S., F. Krumeich, and J.L. Rupp, *A shortcut to garnet-type fast Li-ion conductors for all-solid state batteries*. Journal of Materials Chemistry A, 2015. **3**(36): p. 18636-18648.
106. Gu, W., et al., *Effects of penta-and trivalent dopants on structure and conductivity of Li₇La₃Zr₂O₁₂*. Solid State Ionics, 2015. **274**: p. 100-105.
107. Bernstein, N., M. Johannes, and K. Hoang, *Origin of the structural phase transition in Li₇La₃Zr₂O₁₂*. Physical review letters, 2012. **109**(20): p. 205702.
108. Hu, S., et al., *Structure and ionic conductivity of Li₇La₃Zr₂ - xGexO₁₂ garnet-like solid electrolyte for all solid state lithium ion batteries*. Ceramics International, 2018. **44**(6): p. 6614-6618.
109. Li, Y., et al., *Optimizing Li⁺ conductivity in a garnet framework*. Journal of Materials Chemistry, 2012. **22**(30): p. 15357-15361.
110. Ngo, T.D., et al., *Additive manufacturing (3D printing): A review of materials, methods, applications and challenges*. Composites Part B: Engineering, 2018. **143**: p. 172-196.
111. Ambrosi, A. and M. Pumera, *3D-printing technologies for electrochemical applications*. Chemical Society Reviews, 2016. **45**(10): p. 2740-2755.
112. Tian, X., et al., *Emerging 3D - printed electrochemical energy storage*

- devices: a critical review*. *Advanced Energy Materials*, 2017. **7**(17): p. 1700127.
113. Guo, N. and M.C. Leu, *Additive manufacturing: technology, applications and research needs*. *Frontiers of mechanical engineering*, 2013. **8**(3): p. 215-243.
114. Chang, P., et al., *3D printed electrochemical energy storage devices*. *Journal of Materials Chemistry A*, 2019. **7**(9): p. 4230-4258.
115. Ngo, T.D., et al., *Additive manufacturing (3D printing): A review of materials, methods, applications and challenges*. *Composites Part B: Engineering*, 2018. **143**: p. 172-196.
116. Ghadkolai, M.A., et al., *Freeze tape cast thick Mo doped Li₄Ti₅O₁₂ electrodes for lithium-ion batteries*. *Journal of The Electrochemical Society*, 2017. **164**(12): p. A2603.
117. Porz, L., et al., *Dislocations in ceramic electrolytes for solid-state Li batteries*. *Scientific Reports*, 2021. **11**(1): p. 1-8.
118. Ho, C.C., J.W. Evans, and P.K. Wright, *Direct write dispenser printing of a zinc microbattery with an ionic liquid gel electrolyte*. *Journal of Micromechanics and Microengineering*, 2010. **20**(10): p. 104009.
119. Fu, K., et al., *Graphene oxide-based electrode inks for 3D-printed lithium-ion batteries*. *Advanced Materials*, 2016. **28**(13): p. 2587-2594.
120. Blake, A.J., et al., *3D printable ceramic-polymer electrolytes for flexible high - performance li - ion batteries with enhanced thermal stability*.

- Advanced energy materials, 2017. **7**(14): p. 1602920.
121. McOwen, D.W., et al., *3D-Printing Electrolytes for Solid-State Batteries*. Advanced Materials, 2018. **30**(18): p. 1707132.
122. Eckel, Z.C., et al., *Additive manufacturing of polymer-derived ceramics*. Science, 2016. **351**(6268): p. 58-62.
123. Santoliquido, O., P. Colombo, and A. Ortona, *Additive Manufacturing of ceramic components by Digital Light Processing: A comparison between the "bottom-up" and the "top-down" approaches*. Journal of the European Ceramic Society, 2019. **39**(6): p. 2140-2148.
124. Chartrain, N.A., C.B. Williams, and A.R. Whittington, *A review on fabricating tissue scaffolds using vat photopolymerization*. Acta biomaterialia, 2018. **74**: p. 90-111.
125. Manapat, J.Z., et al., *3D printing of polymer nanocomposites via stereolithography*. Macromolecular Materials and Engineering, 2017. **302**(9): p. 1600553.
126. Kim, S.-H., et al., *Printable solid-state lithium-ion batteries: a new route toward shape-conformable power sources with aesthetic versatility for flexible electronics*. Nano letters, 2015. **15**(8): p. 5168-5177.
127. Chen, Q., et al., *Printing 3D gel polymer electrolyte in lithium-ion microbattery using stereolithography*. Journal of The Electrochemical Society, 2017. **164**(9): p. A1852.
128. Zekoll, S., et al., *Hybrid electrolytes with 3D bicontinuous ordered ceramic*

- and polymer microchannels for all-solid-state batteries.* Energy & Environmental Science, 2018. **11**(1): p. 185-201.
129. Reyes, C., et al., *Three-dimensional printing of a complete lithium ion battery with fused filament fabrication.* ACS Applied Energy Materials, 2018. **1**(10): p. 5268-5279.
130. Smith, A., et al., *Precision measurements of the coulombic efficiency of lithium-ion batteries and of electrode materials for lithium-ion batteries.* Journal of The Electrochemical Society, 2009. **157**(2): p. A196.
131. Xu, C., *Screen Printing and Rheology of Pastes.* 2019: Karlsruher Institut für Technologie (KIT).
132. Shen, F., et al., *A Simple and Highly Efficient Method toward High-Density Garnet-Type LLZTO Solid-State Electrolyte.* ACS Applied Materials & Interfaces, 2020. **12**(27): p. 30313-30319.
133. Badami, P., et al., *Highly Conductive Garnet-Type Electrolytes: Access to $\text{Li}_{6.5}\text{La}_3\text{Zr}_{1.5}\text{Ta}_{0.5}\text{O}_{12}$ Prepared by Molten Salt and Solid-State Methods.* ACS Applied Materials & Interfaces, 2020. **12**(43): p. 48580-48590.
134. Koos, E. and N. Willenbacher, *Capillary forces in suspension rheology.* Science, 2011. **331**(6019): p. 897-900.
135. Thomas, A., B. Matthäus, and H.-J. Fiebig, *Fats and Fatty Oils*, in *Ullmann's Encyclopedia of Industrial Chemistry.* 2015. p. 1-84.
136. Massing, U., S. Cicko, and V. Ziroli, *Dual asymmetric centrifugation (DAC)—A new technique for liposome preparation.* Journal of Controlled Release,

2008. **125**(1): p. 16-24.
137. Sun, H., Z. Han, and N. Willenbacher, *Ultrastretchable conductive elastomers with a low percolation threshold for printed soft electronics*. ACS applied materials & interfaces, 2019. **11**(41): p. 38092-38102.
138. Maurath, J., *Tailored Formulation of Capillary Suspensions as Precursor for Porous Sintered Materials*. 2018.
139. Yüce, C., et al., *Non-volatile free silver paste formulation for front-side metallization of silicon solar cells*. Solar energy materials & solar cells, 2019. **200**: p. Article-No.
140. Maurath, J., *Tailored Formulation of Capillary Suspensions as Precursor for Porous Sintered Materials*. 2018: Karlsruher Institut für Technologie (KIT).
141. Barnes, H. and J. Carnali, *The vane-in-cup as a novel rheometer geometry for shear thinning and thixotropic materials*. Journal of rheology, 1990. **34**(6): p. 841-866.
142. Yüce, C. and N. Willenbacher, *Challenges in rheological characterization of highly concentrated suspensions—A case study for screen-printing silver pastes*. JoVE (Journal of Visualized Experiments), 2017(122): p. e55377.
143. Oswald, W. and N. Willenbacher, *Controlling elongational flow behavior of low viscosity complex fluids at constant shear viscosity*. Rheol. Acta, 2019. **58**(10): p. 687-698.
144. Macosko, C., *Rheology principles measurements and application*. 1994: Wiley-VCH.

145. Xu, C., M. Fieß, and N. Willenbacher, *Impact of wall slip on screen printing of front-side silver pastes for silicon solar cells*. IEEE Journal of Photovoltaics, 2016. **7**(1): p. 129-135.
146. Hamilton, W., *A technique for the characterization of hydrophilic solid surfaces*. Journal of Colloid and Interface Science, 1972. **40**(2): p. 219-222.
147. Zhang, W. and B. Hallström, *Membrane characterization using the contact angle technique I. methodology of the captive bubble technique*. Desalination, 1990. **79**(1): p. 1-12.
148. Grundke, K., et al., *Liquid-fluid contact angle measurements on hydrophilic cellulosic materials*. Colloids and Surfaces A: Physicochemical and Engineering Aspects, 1996. **116**(1-2): p. 79-91.
149. Koos, E., et al., *Tuning suspension rheology using capillary forces*. Soft Matter, 2012. **8**(24): p. 6620-6628.
150. Dittmann, J. and N. Willenbacher, *Micro Structural Investigations and Mechanical Properties of Macro Porous Ceramic Materials from Capillary Suspensions*. Journal of the American Ceramic Society, 2014. **97**(12): p. 3787-3792.
151. Coussot, P., *Rheometry of pastes, suspensions, and granular materials: applications in industry and environment*. 2005.
152. Koos, E. and N. Willenbacher, *Particle configurations and gelation in capillary suspensions*. Soft Matter, 2012. **8**(14): p. 3988-3994.
153. Meeker, S.P., R.T. Bonnecaze, and M. Cloitre, *Slip and flow in soft particle*

- pastes*. Physical Review Letters, 2004. **92**(19): p. 198302.
154. Meeker, S.P., R.T. Bonnecaze, and M. Cloitre, *Slip and flow in pastes of soft particles: Direct observation and rheology*. Journal of Rheology, 2004. **48**(6): p. 1295-1320.
155. Murugan, R., V. Thangadurai, and W. Weppner, *Fast Lithium Ion Conduction in Garnet-Type $\text{Li}_7\text{La}_3\text{Zr}_2\text{O}_{12}$* . Angewandte Chemie International Edition, 2007. **46**(41): p. 7778-7781.
156. Maurath, J. and N. Willenbacher, *3D printing of open-porous cellular ceramics with high specific strength*. Journal of the European Ceramic Society, 2017. **37**(15): p. 4833-4842.

